ARTICLES
https://doi.org/10.1038/s41565-020-00836-6
nature nanotechnology

Check for updates

Hepatic macrophages act as a central hub for relaxin-mediated alleviation of liver fibrosis

Mengying Hu[1], Ying Wang[1], Zhengsheng Liu[1], Zhuo Yu[1], Kaiyun Guan[1], Mengrui Liu[1], Menglin Wang[1], Jun Tan[2] and Leaf Huang[1]✉

Relaxin is an antifibrotic peptide hormone previously assumed to directly reverse the activation of hepatic stellate cells for liver fibrosis resolution. Using nanoparticle-mediated delivery, here we show that, although relaxin gene therapy reduces liver fibrosis in vivo, in vitro treatment fails to induce quiescence of the activated hepatic stellate cells. We show that hepatic macrophages express the primary relaxin receptor, and that, on relaxin binding, they switch from the profibrogenic to the pro-resolution phenotype. The latter releases exosomes that promote the relaxin-mediated quiescence of activated hepatic stellate cells through miR-30a-5p. Building on these results, we developed lipid nanoparticles that preferentially target activated hepatic stellate cells in the fibrotic liver and encapsulate the relaxin gene and miR-30a-5p mimic. The combinatorial gene therapy achieves synergistic antifibrosis effects in models of mouse liver fibrosis. Collectively, our findings highlight the key role that macrophages play in the relaxin-primed alleviation of liver fibrosis and demonstrate a proof-of-concept approach to devise antifibrotic strategies through the complementary application of nanotechnology and basic science.

Activated hepatic stellate cells (aHSCs) are the main effector cells for liver fibrosis via the production of excessive extracellular matrix (ECM) in response to chronic liver injuries. Recent evidence indicated that aHSCs can be reversed to a quiescent phenotype in vivo, which contributes to the resolution of liver fibrosis[1]. Our previous study demonstrated the association between a spontaneous resolution of liver fibrosis with an endogenous peptide hormone, relaxin (RLN)[2]. Upregulation of the relaxin receptor family peptide-1 (RXFP1) on aHSCs facilitates RLN binding and the reversion to quiescence. Although the exogenous introduction of RLN has been proved to deactivate aHSCs in the diseased liver[2,3], the exact underlying mechanism remains unclear.

Besides aHSCs, macrophages are implicated as a 'double-edge sword' in fibrogenesis[4,5], which suggests a potential interaction between the two cell types during the progression and resolution of liver fibrosis. Macrophages possess phenotypic plasticity in response to environmental cues. Bone-marrow-derived Ly6C high expression (Ly6C^{hi}) macrophages predominate the macrophage population in the injured liver. This subtype of hepatic macrophage is inflammatory and critical for hepatic stellate cell (HSC) activation via the production of profibrogenic factors, such as transforming growth factor-β (TGF-β) and platelet-derived growth factor (PDGF)[6]. The Ly6C^{hi} macrophages undergo a phenotype switch into the Ly6C low expression (Ly6C^{lo}) subset during fibrosis resolution, which has been characterized by the upregulation of matrix metalloproteinases (MMPs) and downregulation of inflammatory cytokines[5]. However, whether these properties render Ly6C^{lo} macrophages competent in resolving fibrosis remains to be defined. And a more detailed understanding of the specific mechanisms that govern the macrophage phenotype switch and subsequent interaction with aHSCs for the regression of liver fibrosis will probably inform novel antifibrosis strategies.

Here, we found that, despite the potent antifibrosis efficacy of enforced RLN expression within the fibrotic liver in vivo, in vitro treatment of aHSCs with RLN failed to deactivate the cells or reduce ECM deposition. This discrepancy suggests the microenvironment that surrounds aHSCs contributed to the RLN-mediated antifibrosis effect, which then triggered our discovery of the surface expression of RXFP1 on hepatic macrophages. The binding of RLN to RXFP1 promoted a macrophage phenotype switch from Ly6C^{hi} to Ly6C^{lo} via the activation of an orphan nuclear receptor, Nur77. The hepatic macrophage depletion and in vitro co-culture system proves the essential role of Ly6C^{lo} macrophages as intermediates for RLN-regulated aHSC deactivation. We further demonstrated that exosomes released from these macrophages were responsible for mediating the cross-talk between macrophages and aHSCs. Specifically, microRNA (miRNA) profiling of exosomes derived from RLN-treated macrophages shows upregulation of miR-30a-5p, which, once taken up by aHSCs, targets apoptosis signal-regulating kinase 1 (ASK1) and can overcome a deficiency of peroxisome proliferator-activated receptor-γ (PPAR-γ) caused by the profibrogenic activation in aHSCs. Upregulation of PPAR-γ expression eventually sensitizes aHSCs to RLN-mediated deactivation. Finally, we validated that the targeted delivery of miR-30a-5p towards aHSCs synergizes RLN gene therapy and the combinatorial gene therapy achieves an enhanced antifibrosis effect in multiple liver fibrosis models.

Discrepant in vivo and in vitro antifibrosis effects of RLN

An experimental liver fibrosis model was established by a 6-week-administration of carbon tetrachloride (CCl_4) and monitored by hepatic echogenicity, in which the reflection of ultrasound waves at the interface with a changed stiffness corresponds to the brightness in the ultrasound image[7]. RLN treatments began after four weeks of CCl_4 injection, when moderate liver fibrosis had developed (Fig. 1a–c). Although continuous infusion of recombinant RLN was previously reported to reduce myofibroblasts[3], daily intravenous (i.v.) injection of the peptide for two weeks did not slow down the progression of liver fibrosis (Fig. 1b,c), presumably due to the short half-life[8] and widely expressed RXFP1[9]. To solve the problem,

[1]Division of Pharmacoengineering and Molecular Pharmaceutics, Eshelman School of Pharmacy, University of North Carolina, Chapel Hill, NC, USA. [2]Department of Hepatology, HwaMei Hospital, University of Chinese Academy of Sciences, Ningbo, P.R. China. ✉e-mail: leafh@email.unc.edu

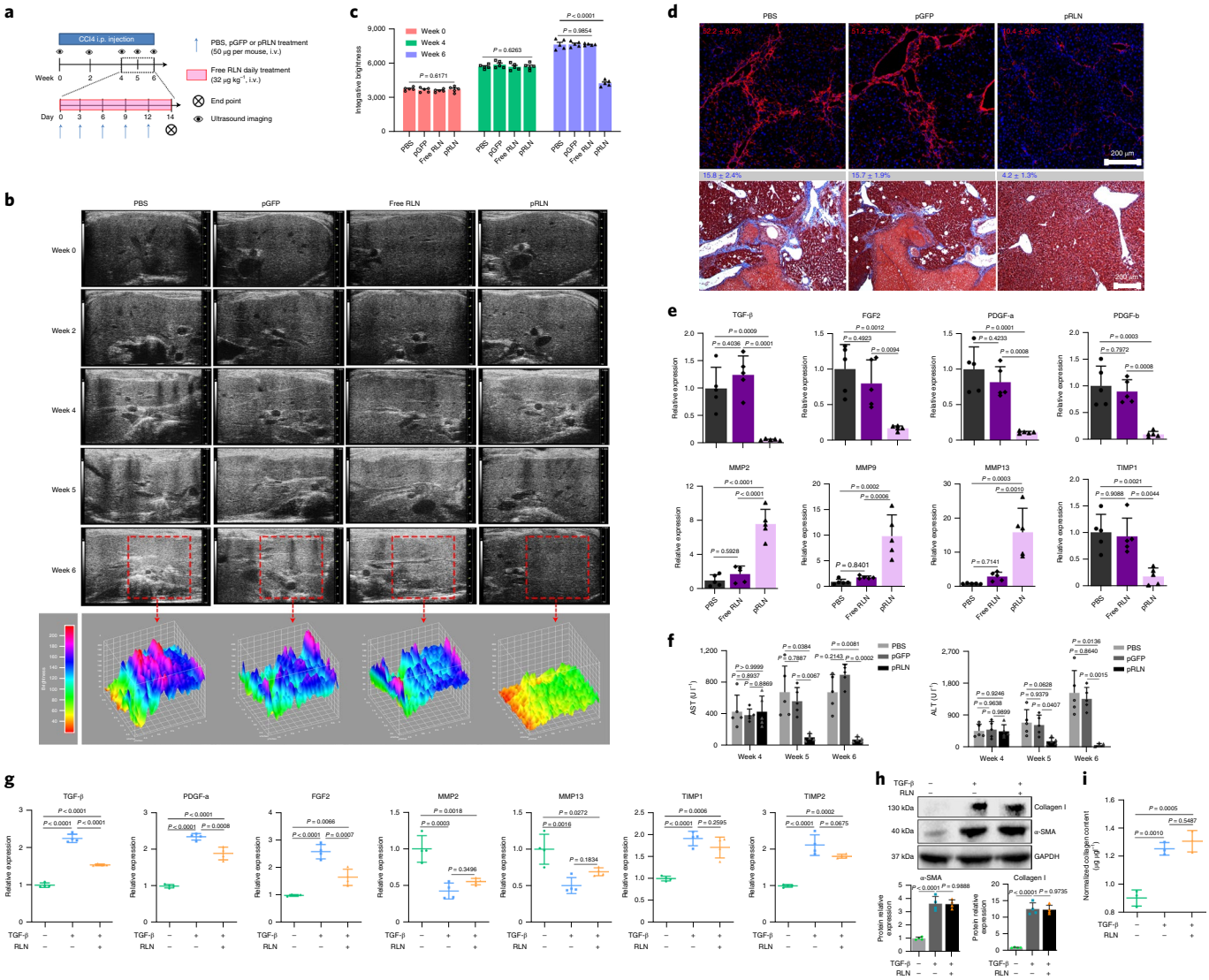

Fig. 1 | Discrepancy between the in vivo and in vitro antifibrosis effects of RLN. a, Schematic representation of the CCl_4-induced liver fibrosis model and treatment timeline for PBS, pGFP LPD, pRLN LPD or free RLN therapy. **b**, Representative in vivo ultrasound imaging of mice livers from different treatment groups before and 2, 4, 5 and 6 weeks after the initiation of CCl_4 injections. Fibrosis development can be seen by an increased intensity and heterogeneity in hepatic echogenicity. The 3D surface plots of the ultrasound images within the red dashed squares at week 6 after the initiation of CCl_4 injections correspond to the echogenic uniformity in the liver. **c**, Quantification analysis of liver fibrosis severity by the integrated intensity of echogenicity (image brightness) ($n = 5$ biologically independent mice per group). **d**, Representative immunofluorescence staining of α-SMA (top) and Masson's trichrome (bottom) in CCl_4-induced fibrotic livers from the PBS, pGFP LPD and pRLN LPD treatment groups. Red and blue numbers indicate the average % of α-SMA-positive cells (upper panel) and the average % collagen coverage (lower panel), respectively, quantified in five randomly selected fields per mouse ($n = 5$ biologically independent mice per group). $^{****}P < 0.0001$ for pRLN versus PBS comparison. **e**, Relative mRNA expression of TGF-β, FGF2, PDGF-a/b, MMP2, MMP9, MMP13 and TIMP1 in CCl_4-induced fibrotic livers from the PBS, recombinant RLN (free RLN) and pRLN LPD treatment groups ($n = 5$). **f**, Liver injury characterization by serum ALT and AST in mice from the PBS, recombinant RLN and pRLN LPD treatment groups at weeks 4, 5 and 6 after the initiation of CCl_4 injections ($n = 5$ biologically independent mice per group). **g**, Relative mRNA expression of TGF-β, FGF2, PDGF-a, MMP2, MMP13, TIMP1 and TIMP2 after RLN treatment (100 ng ml^{-1}) in TGF-β (10 ng ml^{-1})-activated HSC-T6 cells ($n = 4$ biologically independent samples per group). **h**, Western blot analysis of α-SMA and collagen I expression after RLN treatment in TGF-β-activated HSC-T6 cells. Data shown represent one of four independent samples with similar results. Cumulative densitometric analyses of the western blotting images were performed by ImageJ ($n = 4$ biologically independent samples per group). **i**, Total collagen production after RLN treatment in TGF-β-activated HSC-T6 cells measured by a Sirius Red detection assay ($n = 3$ biologically independent samples per group). Both in vitro and in vivo experiments were repeated twice independently with similar results. **c**–**i**, Significant differences were assessed using a two-way analysis of variance (ANOVA) with Turkey test (**c**,**f**) and a one-way ANOVA with Turkey test (**d**,**e**,**g**–**i**). Results are presented as mean ± standard deviation (s.d.) from the second repeat. i.p., intraperitoneal injection.

an in situ RLN depot within the fibrotic lesions was designed via the targeted delivery of plasmid DNA (pDNA) that encoded RLN (pRLN) using lipid–protamine–DNA (LPD) nanoparticles conjugated with aminoethyl anisamide (AEAA), a potent ligand for the sigma-1 receptor, which was highly expressed on aHSCs[2]. About a 20-fold upregulation of RLN was only detected in the liver, but not in any other major organs or serum after the pRLN LPD injections (Supplementary Fig. 1a), which proves liver-specific gene

expression. The delivery of the pDNA-encoding green fluorescent protein (pGFP) using the same delivery system further confirmed ~20% transfection efficacy and α-SMA$^+$ (the single most reliable aHSC marker[10]) cells as the predominantly transfected cells in the fibrotic liver (Supplementary Fig. 1b). Consistent with the murine system, the sigma-1 receptor was also detected on human HSCs (Supplementary Fig. 2a,b), which suggests the translational potential of the gene delivery system. Remarkably, two weeks of treatment with pRLN LPD reversed the liver fibrosis, as characterized by a reduced and more homogeneous echo intensity (Fig. 1a–c), and downregulated the intrahepatic α-SMA expression and collagen (a major ECM protein) deposition (Fig. 1d and Supplementary Fig. 3) compared with those in the PBS or pGFP LPD treatment groups. Furthermore, we found a substantial reduction of profibrogenic factors, which included TGF-β (~20-fold), PDGF-a/b (about tenfold) and fibroblast growth factor 2 (FGF2) (~6-fold), along with upregulation of MMPs, such as MMP2, MMP9 and MMP13, and downregulation of the tissue inhibitor of metalloproteinase 1 (TIMP1) (~6-fold) in livers of mice treated with pRLN LPD compared with the up- and downregulations of PBS-treated livers (Fig. 1e). Alanine aminotransferase (ALT) and aspartate transaminase (AST) are two major liver enzymes released into blood on liver injuries. The normalization of the serum level for both enzymes was only achieved by the pRLN LPD treatment (Fig. 1f). The antifibrosis effect of the RLN gene therapy was further examined in mice fed with a methionine-choline-deficient (MCD) diet (Supplementary Fig. 4a), which causes non-alcoholic steatohepatitis that accompanies liver fibrosis. Similar to the CCl_4-induced liver fibrosis model, pRLN LPD treatments decreased the α-SMA expression and collagen content in the liver and gradually alleviated the serum ALT and AST levels (Supplementary Fig. 4b–d).

In vitro stimulation of rat HSC-T6 cells as well as of human primary HSCs and LX-2 cells by TGF-β increased the expression of profibrogenic factors, TIMPs, α-SMA and collagen, but decreased MMP levels compared with those in unstimulated cells (Fig. 1g–i and Supplementary Fig. 6), which closely mimics the in vivo activation of HSCs. Consistent with the literature[2,3], RXFP1 (the primary RLN receptor) expression was detected on all the HSC cultures, and was slightly increased in response to TGF-β activation (Supplementary Fig. 5). Therefore, we presumed RLN exerted the antifibrosis effect via direct deactivation of aHSCs after binding with RXFP1. Unexpectedly, the RLN treatment only slightly downregulated mRNA levels of profibrogenic factors (Fig. 1g), but did not reduce α-SMA expression or collagen production in activated HSC-T6 (Fig. 1h,i). Similarly, there were no differences in the mRNA expression of α-SMA (ACTA2), type I collagen (COL1A1), profibrogenic factors, MMP1 or TIMP1 in activated human primary HSCs and LX-2 cells between the PBS and RLN treatments (Supplementary Fig. 6). The discrepant in vivo and in vitro aHSC deactivation effect implies an important contribution of the microenvironment that surrounds aHSCs (for example, macrophages) to the RLN-mediated antifibrosis effect.

RLN drives macrophage phenotype switch

In addition to aHSCs, we found that a majority of macrophages expressed RXFP1 in both mouse and human fibrotic livers (Supplementary Fig. 7a,b). Specifically, Ly6C^{hi} pro-inflammatory macrophages, differentiated from bone-marrow-derived monocytes, dominated the hepatic macrophage population in mouse chronically inflamed and fibrotic livers[6,11]. As the fibre resolution started, these Ly6c^{hi} macrophages phenotypically switched to the Ly6C^{lo} subset, which became the dominant population at the maximal resolution of liver fibrosis[5]. Interestingly, more than a fivefold increase of RXFP1 expression was detected on fluorescence-activated cell sorted (FACS) Ly6C^{hi} macrophages compared with that on Ly6C^{lo} macrophages in CCl_4-induced fibrotic livers (Supplementary Fig. 8). The association of a higher surface expression of RXFP1 with a pro-inflammatory phenotype primed by interferon-γ (IFN-γ) and lipopolysaccharide (LPS) stimulation was also found on in vitro cultured bone-marrow-derived macrophages (BMDMs) (Supplementary Fig. 9a,b) and Raw264.7 cells (Supplementary Fig. 9c,d).

Corresponding to RXFP1 expression on macrophages, the RLN gene therapy significantly regulated macrophage-associated genes in CCl_4-induced fibrotic livers (Fig. 2a). For instance, monocyte recruitment chemokines, CCL2 and CCL5, were upregulated in response to the RLN treatment (Fig. 2a). Notably, a higher expression of mannose receptor 1 (MRC1), a signature for pro-resolution macrophages[5,12,13], but about a tenfold lower expression of Ly6C were observed after the RLN gene therapy compared with those after PBS treatment (Fig. 2a), which suggests an overall change in macrophage phenotype. Flow cytometric analysis of Ly6C expression on hepatic macrophages identified a change in the Ly6C^{lo}/Ly6C^{hi} ratio from 1.0 in the PBS control mice to 3.2 after pRLN LPD treatments (Figs. 2b and 3b). In vitro treatment of IFN-γ + LPS-stimulated BMDM with RLN peptide also demonstrated downregulated Ly6C and CD86 (another marker for pro-inflammatory macrophages[5,14,15]) as well as TGF-β and TIMP1, and upregulated MRC1 and MMP9 expressions, which suggests reversion of the pro-inflammatory phenotypic switch (Fig. 2c,d). A similar RLN-mediated regulation on phenotype- and/or fibrogenesis-associated genes was also found in Raw264.7 cells (Supplementary Fig. 10). To determine whether a RLN-induced phenotype switch in macrophages is through RXFP1/RLN interaction, RXFP1 was knocked down by short interfering RNA (siRNA) specific to RXFP1 (siRXFP1) in Raw264.7 cells (Supplementary Fig. 11a). Although RLN treatment decreased the mRNA expressions of Ly6C, CD86 and TIMP1, and increased the MMP9 level in the negative control siRNA (siCtr) group, the regulation effect was abrogated in RXFP1-knockdown cells (Supplementary Fig. 11b), which proved an indispensable role of RXFP1 in a RLN-driven phenotype switch in macrophages. Strongly increased frequencies of intermediate CD14$^+$CD16$^+$ macrophages, which are differentiated from CD14 high expression (CD14^{hi}) CD16$^-$ monocytes, have been recorded in patients with chronic liver diseases[16,17]. These CD14$^+$CD16$^+$ macrophages were found to have HSC-activating capacities and align with Ly6C^{hi} macrophages in mouse fibrotic livers[18]. IFN-γ + LPS stimulation dramatically upregulated CD16 and RXFP1 expressions in human BMDMs (hBMDMs) and slightly downregulated the CD14 level (Supplementary Fig. 12a,b). Although RLN treatment further decreased the mRNA expression of CD14, CD16 was reversely regulated to a level close to that of unstimulated cells (Supplementary Fig. 12a), which indicates that the RLN-mediated phenotype switch also applies to human macrophages.

Nur77 upregulation plays a critical role for the generation and survival of Ly6C^{lo} monocytes[19,20] and its overexpression ameliorates fibrosis in multiple organs, which include the fibrotic liver[21]. Therefore, we next analysed whether Nur77 expression regulates the phenotypic switch in macrophages and whether it is affected by RLN treatment. Although pro-inflammatory stimulation decreased Nur77 expression by 50% in Raw264.7 and BMDMs, RLN treatment upregulated its expression to a level comparable to or even higher than that in unpolarized control cells (Fig. 2e,f). Moreover, the addition of RLN remedied the fraction of Nur77 overlapping with cell nucleus (Fig. 2f). Similar to the in vitro results, a significantly higher expression of Nur77 was observed in FACS hepatic macrophages (Supplementary Fig. 8a) after the RLN gene therapy compared with that after PBS treatment (Fig. 2g,h). More specifically, a >20-fold increase in Nur77 mRNA expression was detected in Ly6C^{lo} macrophages compared with that in the Ly6C^{hi} subset (Fig. 2i). The upregulation and translocation of Nur77 from the cytoplasm to the nucleus suggests its activation in macrophages, which may be associated with a RLN-induced pro-resolution phenotype switch.

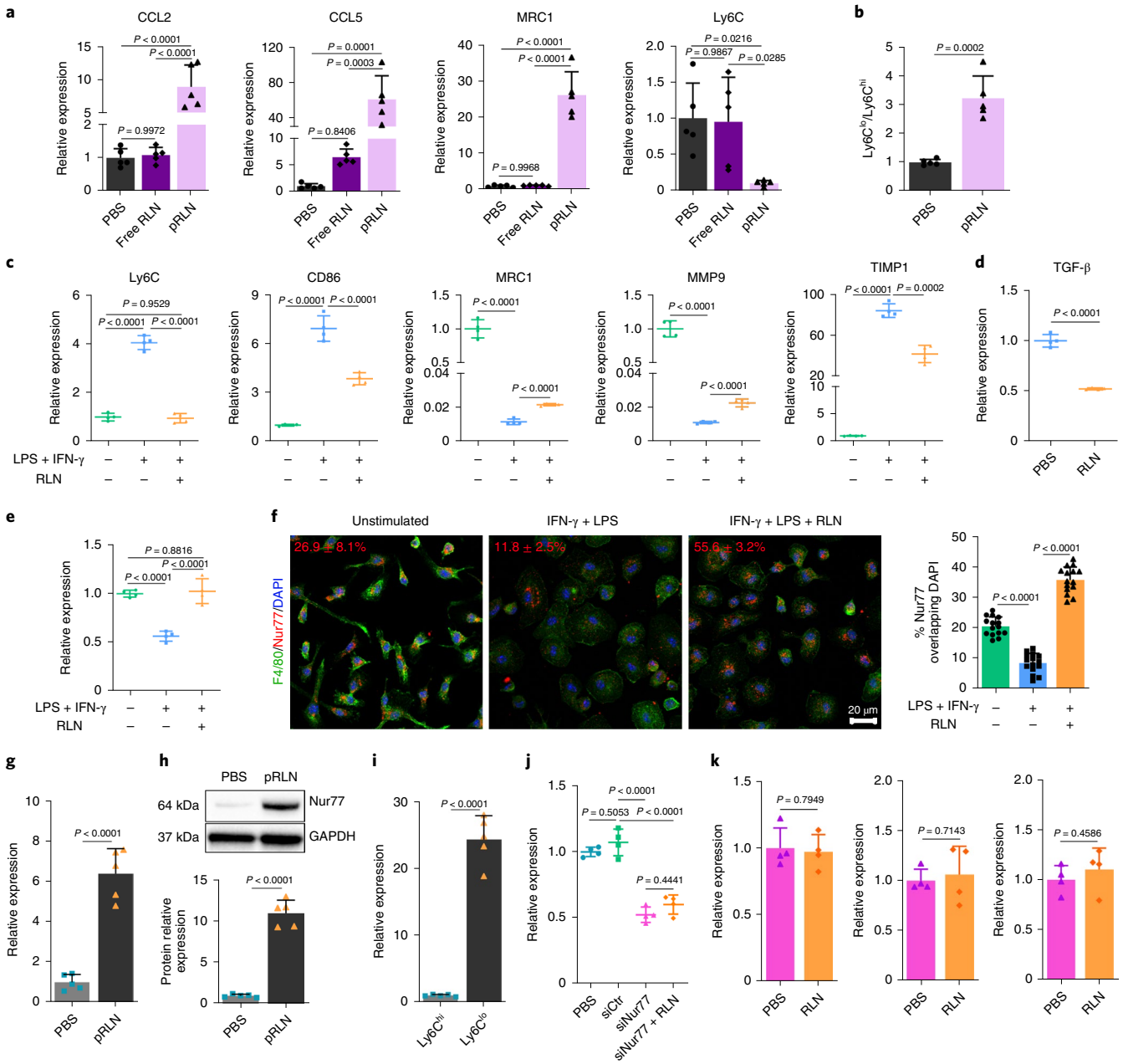

Fig. 2 | RLN treatment drives the macrophage phenotype switch via Nur77 activation. **a**, Relative mRNA expression of MRC1, Ly6C, CCL2 and CCL5 in CCl_4-induced fibrotic livers from PBS, recombinant RLN and pRLN LPD treatment groups ($n = 5$ biologically independent mice per group). **b**, The ratio of $Ly6C^{lo}$ macrophages to $Ly6C^{hi}$ macrophages in CCl_4-induced fibrotic livers after PBS or pRLN LPD treatments by flow cytometry analysis ($n = 5$ biologically independent mice per group). **c**, Relative mRNA expression of Ly6C, CD86, MRC1, MMP9 and TIMP1 in BMDMs with or without LPS (100 ng ml^{-1}) + IFN-γ (50 ng ml^{-1}) stimulation and RLN treatment (100 ng ml^{-1}) ($n = 4$ biologically independent samples per group). **d** Relative mRNA expression of TGF-β after RLN treatment in BMDMs ($n = 4$ biologically independent samples per group). **e**, Relative mRNA expression of Nur77 in BMDMs with or without LPS + IFN-γ stimulation and RLN treatment ($n = 4$ biologically independent samples per group). **f**, Representative immunofluorescence staining of Nur77 and F4/80 in BMDMs with or without LPS + IFN-γ stimulation and RLN treatment. Red numbers indicate the level of total Nur77 expression normalized by DAPI (4,6-diamidino-2-phenylindole) after different treatments. The quantification of total Nur77 expression and % Nur77 expression in the cell nucleus (right) was performed in five randomly selected fields per sample by ImageJ ($n = 3$ biologically independent samples per group). **g**, Relative mRNA expression of Nur77 in FACS macrophages from CCl_4-induced fibrotic livers of PBS and pRLN LPD treatment groups ($n = 5$ biologically independent mice per group). **h**, Western blot analysis of Nur77 expression in FACS macrophages from CCl_4-induced fibrotic livers of PBS and pRLN LPD treatment groups. Cumulative densitometric analyses of the western blotting images were performed by ImageJ ($n = 5$ biologically independent mice per group). **i**, Relative mRNA expression of Nur77 in FACS $Ly6C^{hi}$ and $Ly6C^{lo}$ macrophages from pRLN-treated fibrotic livers ($n = 5$ biologically independent mice per group). **j**, Relative mRNA expression of Nur77 in Raw264.7 cells without treatment (PBS), transfected with scrambled siCtr or siNur77, or with the combination treatment of siNur77 + RLN ($n = 4$ biologically independent samples per group). **k**, Relative mRNA expression of Ly6C (left), MRC1 (middle) and MMP9 (right) in Nur77-knockdown Raw264.7 cells after PBS or RLN treatment ($n = 4$ biologically independent samples per group). Both in vitro and in vivo experiments were repeated twice independently with similar results. **a**–**k**, Significant differences were assessed using a one-way ANOVA with Turkey test (**a**,**c**,**e**,**f**,**j**) and a two-tailed unpaired Student's *t* test (**b**,**d**,**g**–**i**,**k**). Results are presented as mean ± s.d.) from the second repeat. Cy7, cyanine 7.

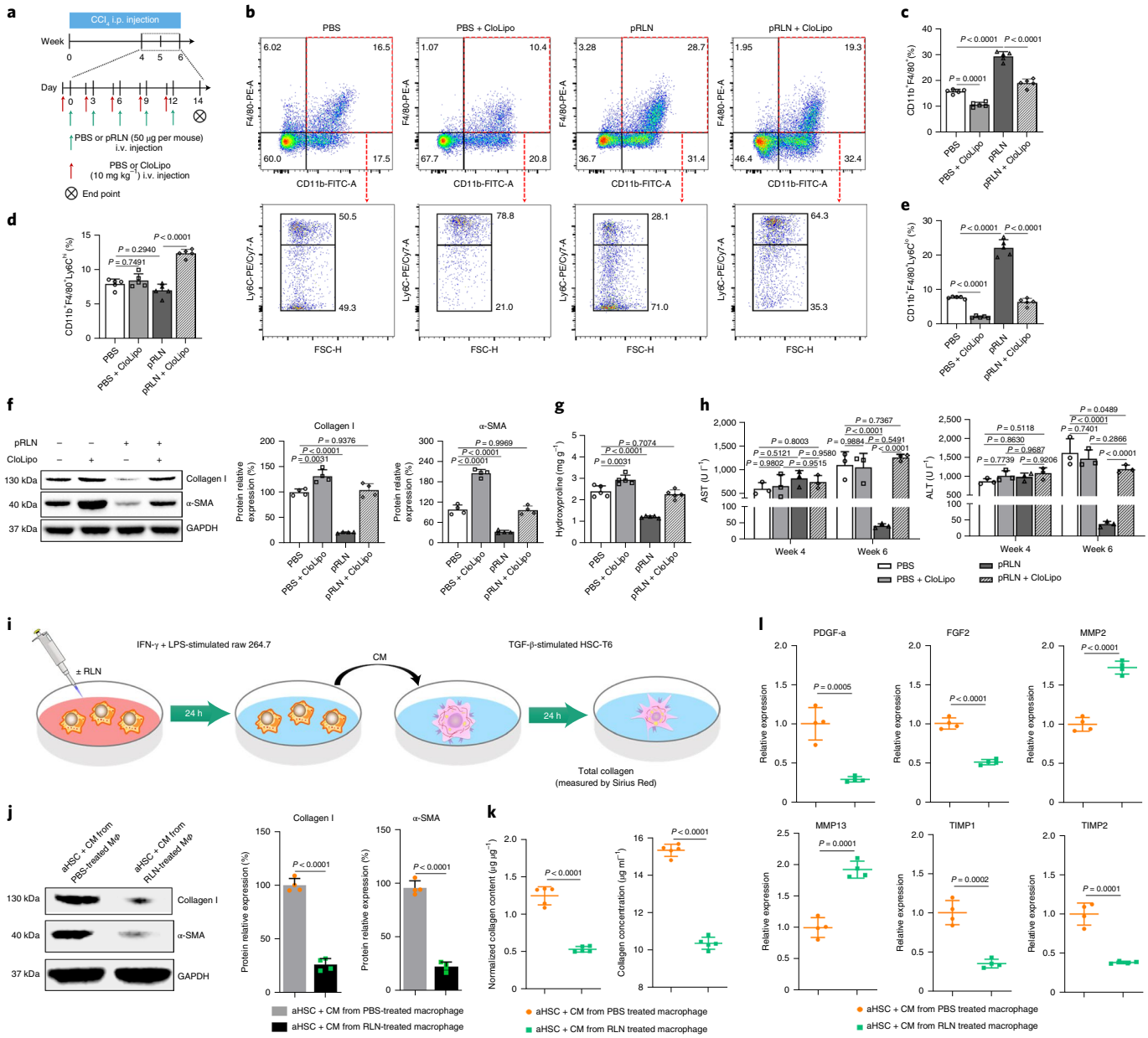

Fig. 3 | Key role of macrophages in RLN-mediated aHSC deactivation. a, Schematic representation of the CCl_4-induced liver fibrosis model, macrophage depletion by CloLipo injections and treatment timeline for PBS and pRLN LPD therapy. **b**–**e**, Representative flow cytometry results (PE-A, phycoerythrin fluorescence intensity; FITC-A, fluorescein isothiocyanate fluorescence intensity; PE/Cy7-A, PE/cyanine7 fluorescence intensity; FSC-H, forward scatter-height.) (**b**) and percentages of $CD11b^+F4/80^+$ total macrophages (**c**) as well as $Ly6C^{hi}$ (**d**) and $Ly6C^{lo}$ (**e**) macrophage subsets in CCl_4-induced fibrotic livers after various treatments ($n = 5$ biologically independent mice per group). **f**, Western blot analysis of α-SMA and collagen I expression in fibrotic livers after various treatments. Cumulative densitometric analyses of the western blotting images were performed by ImageJ ($n = 4$ biologically independent mice per group). **g**, Quantification of hepatic hydroxyproline content. The data are expressed as hydroxyproline (mg) per liver wet weight (g) ($n = 5$ biologically independent mice per group). **h**, Liver injury characterization by serum AST (left) and ALT (right) in mice that received various treatments at weeks 4 and 6 after the initiation of CCl_4 injections ($n = 5$ biologically independent mice per group). **i**, Schematic representation of the in vitro mimicry of the interaction between pro-inflammatory macrophages and TGF-β-activated HSCs. **j**, Western blot analysis of α-smooth muscle actin (α-SMA) and collagen I expression in activated HSC-T6 cells after treatment with CM from Raw264.7 cells treated with either PBS or RLN (100 ng m^{-1}). Cumulative densitometric analyses of the western blotting images were performed by ImageJ ($n = 4$ biologically independent samples per group). **k**, Total collagen measurement in cell lysis (left) or culture medium (right) of activated HSC-T6 cells by a Sirius Red detection assay after treatment with CM from either PBS- or RLN-treated Raw264.7 cells ($n = 5$ biologically independent samples per group). **l**, Relative mRNA expression of PDGF-a, FGF2, MMP2, MMP13, TIMP1 and TIMP2 in activated HSC-T6 cells after treatment with CM from either PBS or RLN Raw264.7 cells ($n = 4$ biologically independent samples per group). Both in vitro and in vivo experiments were repeated twice independently with similar results. Significant differences were assessed in using a one-way ANOVA with Turkey test (**c**–**g**), a two-way ANOVA with Turkey test (**h**) and a two-tailed unpaired Student's *t*-test. Results are presented as mean ± s.d. from the second repeat.

To verify the hypothesis, Nur77 knockdown was performed in Raw264.7 cells by using siRNA specific to Nur77 (siNur77) (Fig. 2j). RLN-induced upregulation of MRC1 and MMP9 and downregulation of Ly6C was observed in the siCtr-treated Raw264.7 cells, but not in the siNur77 group (Fig. 2k), which indicates the indispensable involvement of Nur77 activation to fulfil the RLN-mediated phenotype switch.

As a G protein-coupled receptor, the activation of RXFP1 by RLN has been tied to an increased cyclic AMP (cAMP) production[22] and an activated downstream cAMP-responsive element-binding (CREB) protein, which upregulates Nur77 expression[23]. We confirmed RLN treatment increased intracellular cAMP (Supplementary Fig. 13a) and phosphorylation of the CREB protein and Nur77 expression (Supplementary Fig. 13b), which was abrogated by RXFP1 knockdown (Supplementary Fig. 11b). Although there was no significant change in protein kinase A (PKA) expression (Supplementary Fig. 13b), an increased PKA activity was observed in RLN-treated cells, which could be blocked by treatment with the PKA inhibitor H89 (Supplementary Fig. 13c). Thus, these data indicate that RLN activates Nur77 in macrophages through a cAMP–PKA–CREB pathway, which promotes the macrophage phenotype switch from profibrogenesis to pro-resolution.

RLN-treated macrophages deactivate aHSCs via exosomal miR-30a-5p

A macrophage-depletion study was then performed to determine the role of macrophage in the RLN-mediated antiliver fibrosis effect (Fig. 3a). A significant reduction of the total hepatic macrophages (Fig. 3b,c and Supplementary Figs. 14 and 15) compared with those in the corresponding controls (PBS + CloLipo versus PBS and pRLN + CloLipo versus pRLN) was confirmed after clodronate liposome (CloLipo) injections. More specifically, the Ly6C^{lo} macrophages, but not the Ly6C^{hi} subset, responded to CloLipo treatments (Fig. 3b,d,e) due to the higher phagocytic capacity of the Ly6C^{lo} population[5]. Consistent with the upregulated expressions of CCL2 and CCL5 (Fig. 2a), an enhanced macrophage infiltration (particularly predominated by the Ly6C^{lo} subset) was observed after the RLN gene therapy. Clec4f^{+} Kupffer cells were negligible (Supplementary Fig. 16) due to the CCl_4-induced liver injury[5,24]. Nevertheless, pRLN treatment slightly increased Kupffer cells, which were presumably repopulated from recruited macrophages after the RLN-driven phenotype switch, which indicates a milder status of liver injury. CloLipo not only offset the RLN-induced upregulation of Ly6C^{lo} macrophages, but completely abrogated the antifibrosis effect of pRLN LPD treatments, as shown by the unchanged expressions of hepatic α-SMA and type I collagen (Fig. 3f and Supplementary Fig. 17), hydroxyproline content (Fig. 3g) or serum AST relative to that of the PBS control (Fig. 3h).

To further define mechanisms involved in the interaction between RLN-induced Ly6C^{lo} macrophages and aHSCs, conditioned medium (CM) from pro-inflammatory Raw264.7 cells with or without RLN treatment was added into the activated HSC-T6 (Fig. 3i). Significant reductions of α-SMA, collagen, profibrogenic factors and TIMPs, and the upregulation of MMPs (Fig. 3j–l) were observed in HSC-T6 cells treated with CM from RLN-treated Raw264.7 cells versus those treated with CM from PBS-treated cells. Changed solubility factors (for example, decreased TGF-β and increased MMP9 secretion (Fig. 2c,d and Supplementary Fig. 10b)) in the CM from RLN-treated macrophages may contribute to the deactivation of aHSCs (Fig. 3j–l). In addition, exosomes are considered important in cell–cell communication, both locally and distantly[25]. To determine the predominant factor that controls the in vitro education of aHSCs, we separately added exosomes (Supplementary Fig. 19) and supernatant from ultracentrifuged Raw264.7 CM into activated HSC-T6. A significant regulation of fibrogenesis-associated genes was only observed after treatment with exosomes derived from RLN-treated Raw264.7 cells (Fig. 4a), which indicates macrophage-derived exosomes, but not secreted factors, such as TGF-β and MMP9, deactivated aHSCs. Successful deactivation of human primary aHSCs (Supplementary Fig. 21) was further confirmed by the treatment of exosomes derived from RLN-treated human peripheral CD14^{int}CD16^{+} cells (a source of profibrogenic macrophages in chronically injured liver[19]), which were FACS from freshly isolated peripheral blood mononuclear cells (Supplementary Fig. 20). Similar results were also validated in activated LX-2/THP-1 macrophage (or hBMDM) systems (Supplementary Figs. 12c and 18). The involvement of macrophage-derived exosomes in the development and/or resolution of liver fibrosis can also be inferred from the peri-aHSC localization of CD63^{+} (a classic exosome marker) macrophages in fibrotic livers (Supplementary Fig. 22), which suggests exosome enrichment in macrophages near fibrotic lesions, but not in those dispersed in fibrosis-free parts. To further testify whether exosomes secreted from RLN-treated macrophages elicit the resolution of liver fibrosis in vivo, 4-week-CCl_4-treated mice were administrated with exosomes isolated from PBS- or RLN-treated Raw264.7 CM (PBS_{exo} or RLN_{exo}) (Fig. 4b). A retarded development of liver fibrosis by RLN_{exo} treatment was verified by reduced hepatic echogenicity, lower serum ALT and AST, and decreased hydroxyproline content and expressions of α-SMA and fibrogenesis-associated genes relative to those of PBS or PBS_{exo} treatment (Fig. 4c–h). Notably, although RLN treatment alone negligibly deactivated aHSCs, combination of RLN_{exo} with RLN synergistically increased MMP13 and reduced FGF2 and TIMP1 expressions in activated HSC-T6 relative to those after PBS treatment (Fig. 4i).

miRNA is among the major exosome cargos responsible for intercellular communication[26,27]. miRNA profiling was thus performed to determine specific exosomal miRNAs derived from RLN-treated macrophages that involved in aHSC deactivation (Fig. 5a). Scatter plots with the boundaries set at plus or minus threefold changes indicated nine highly, but differentially, expressed miRNAs between PBS_{exo} and RLN_{exo} (Fig. 5b). Of the nine miRNAs, six (miR-132-3p, miR-150-5p, miR-27b-3p, miR-30a-5p, miR-378-3p and miR-744-5p) were upregulated and the other three (miR-192-5p, miR-223-3p and miR-25-3p) were downregulated in RLN_{exo} compared with those in PBS_{exo}. A sophisticated database for miRNA target prediction (microRNA Data Integration Portal, http://ophid.utoronto.ca/mirDIP)[28] was used to identify gene targets for the abundant and upregulated exosomal miRNAs. Among the six upregulated miRNAs, miR-30a-5p not only displayed the highest expression level (Fig. 5a,b), but also was predicted to target fibrogenesis-associated genes, such as SMAD1, SMAD2, PDGFa, TIMP2 and TIMP3 with higher integrated scores (Fig. 5c and Supplementary Table 1), which statistically infer a greater potential for miRNA-target interactions[28]. Moreover, miR-30a-5p was predicted to target ASK1 (also known as MAP3K5), a recently identified key facilitator of fibrosis via deregulating the lipid and glucose metabolism[29,30], with an integrated score of more than 0.9. Indeed, a higher miR-30a-5p expression was detected in the liver and FACS hepatic macrophages after the RLN gene therapy compared with that after PBS treatment (Fig. 5d and Supplementary Fig. 23a). Specifically, Ly6C^{lo} macrophages showed a more substantial increase of miR-30a-5p expression relative to that of the Ly6C^{hi} subset (Supplementary Fig. 23b). This effect was abrogated by the CloLipo-induced depletion of Ly6C^{lo} macrophages (Fig. 5d), which indicates that miR-30a-5p upregulation is related to the RLN-mediated phenotype switch of liver macrophages. Consistent with murine macrophages, a significant increase in miR-30a-5p expression in response to RLN treatment was also observed in hBMDMs (Supplementary Fig. 12d).

Downregulated ASK1 and Thr845-phosphorylated ASK1 (pASK1), α-SMA, type I collagen, profibrogenic factors and TIMP1, but upregulated MMPs and PPAR-γ, were detected in LX-2 and

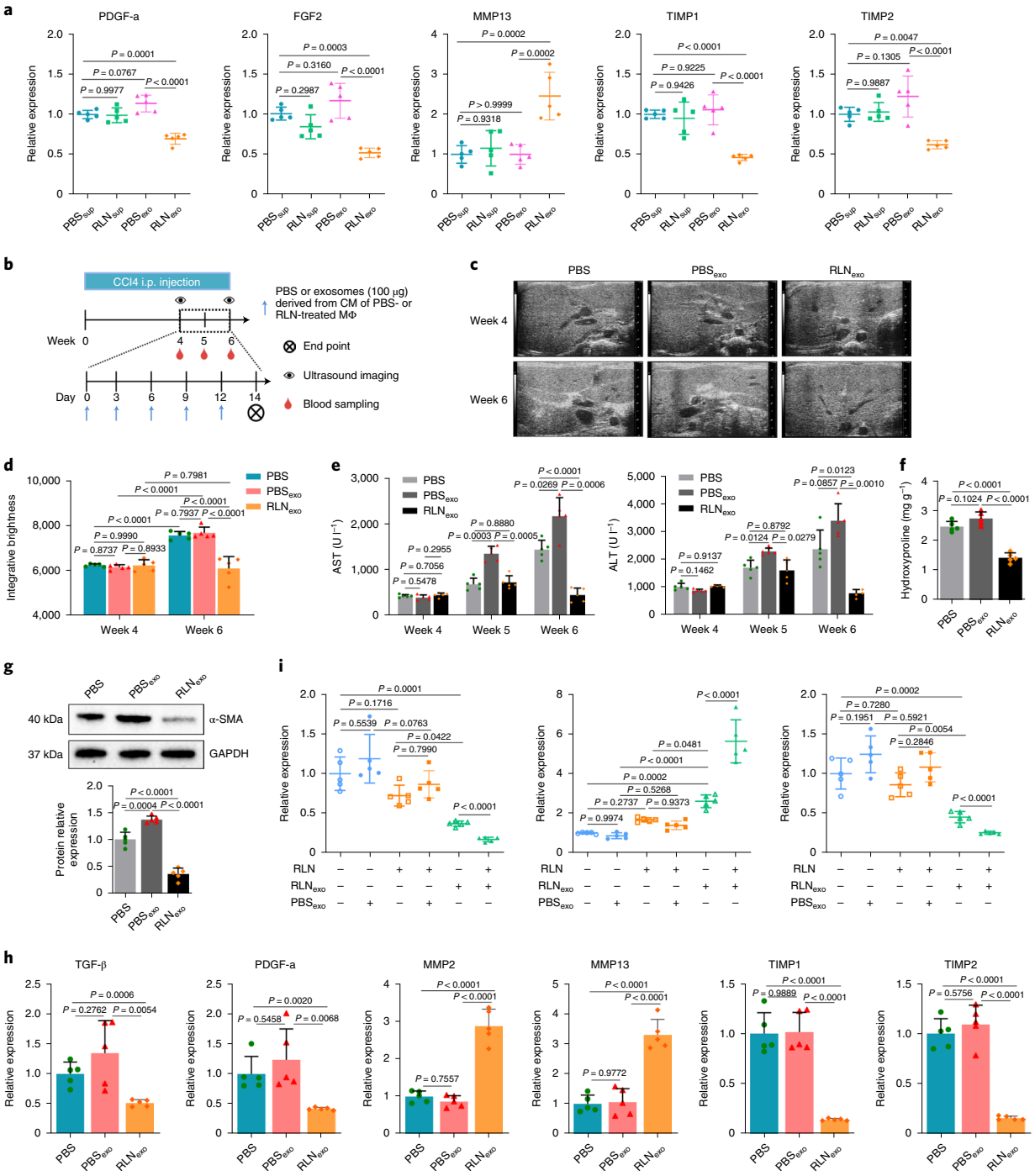

Fig. 4 | RLN-treated macrophages deactivate aHSCs via exosome release. a, Relative mRNA expressions of PDGF-a, FGF2, MMP13, TIMP1 and TIMP2 in activated HSC-T6 cells after treatment with PBS or RLN supernatant (PBS_{sup} or RLN_{sup}) or exosomes (PBS_{exo} and RLN_{exo}) collected via the ultracentrifugation of the CM from either PBS- or RLN-treated Raw264.7 cells ($n=4$ biologically independent samples per group). **b**, Schematic representation of the CCl_4-induced liver fibrosis model and treatment timeline for PBS or exosomes isolated from CM of IFN-γ + LPS stimulated Raw264.7 cells with or without the treatment of RLN. **c**, Representative in vivo ultrasound imaging of mice livers from different treatment groups at weeks 4 and 6 after the initiation of CCl_4 injections. **d**, Quantification analysis of liver fibrosis severity by integrated intensity of echogenicity (image brightness) ($n=5$ biologically independent mice per group). **e**, Liver injury characterization by serum AST (left) and ALT (right) in mice that received various treatments at weeks 4, 5 and 6 after the initiation of CCl_4 injections ($n=5$ biologically independent mice per group). **f**, Quantification of hepatic hydroxyproline content. The data are expressed as hydroxyproline (mg) per liver wet weight (g) ($n=5$ biologically independent mice per group). **g**, Western blot analysis of α-SMA expression in CCl_4-induced fibrotic livers from different treatment groups. Cumulative densitometric analyses of the western blotting images were performed by ImageJ ($n=5$ biologically independent mice per group). **h**, Relative mRNA expression of TGF-β, PDGF-a, MMP2, MMP13, TIMP1 and TIMP2 in CCl_4-induced fibrotic livers from different treatment groups ($n=5$ biologically independent mice per group). **i**, Relative mRNA expression of FGF2 (left), MMP13 (middle) and TIMP1 (right)in activated HSC-T6 cells after treatment with various combinations of RLN (100 ng ml^{-1}) and PBS_{exo} or RLN_{exo} collected from the CM of Raw264.7 cells ($n=4$ biologically independent samples per group). Both in vitro and in vivo experiments were repeated twice independently with similar results. Significant differences were assessed using a two-way ANOVA with Turkey test (**d**,**e**) and a one-way ANOVA with Turkey test (**a**,**f**–**i**). Results are presented as mean ± s.d. from the second repeat.

HSC-T6 cells after miR-30a-5p transfection compared with those in the scrambled-miR (negative control) treatment (Fig. 5e–g and Supplementary Fig. 24), which supports that ectopic expression of miR-30a-5p in aHSCs induces a deactivation effect. Notably, PPAR-γ is a downstream nuclear receptor activated via the signalling pathway initiated by RLN binding with RXFP1[31,32], which then negatively regulates the activation of HSCs[31–33]. Unfortunately, PPAR-γ is dramatically suppressed in myofibroblasts[34], which presumably accounts for the ineffective aHSC deactivation by RLN treatment alone. Although RLN treatment did not change the PPAR-γ expression in aHSCs, RLN + miR-30a-5p substantially increased the nuclear receptor level by about tenfold compared with that of the PBS + scrambled-miR treatment, presumably attributed to ASK1 (a negative regulator of PPAR-γ[35,36]) suppression and associated with a synergistic deactivation of aHSCs (Fig. 5e and Supplementary Fig. 24).

miR-30a-5p knockdown in macrophages was performed to further determine its dominancy in exosomal miRNAs driving aHSC deactivation. A more than 95% downregulation of miR-30a-5p was observed in Raw264.7 after miR-30a-5p hairpin inhibitor (miR30i) transfection relative to that of the miRNA hairpin inhibitor negative control (miRiCtr) or PBS treatment (Fig. 5h). RLN co-treatment with miR30i failed to recover the miR-30a-5p level. As expected, exosomes derived from Raw264.7 cells treated with miR30i + RLN failed to deactivate HSC-T6 relative to those derived from cells treated with miRiCtr + RLN (Fig. 5i,j). Interestingly, miR30i treatment alone led to more profibrogenic exosomes relative to those from miRiCtr treatment. These results indicated that the pro-resolution effect of exosomes derived from RLN-educated macrophages is mainly attributed to miR-30a-5p, which suppresses ASK1 and revives the PPAR-γ activity in aHSCs.

pRLN + miR-30a-5p synergistically reduces liver fibrosis

To verify the antifibrosis effect in vivo, the miR-30a-5p mimic was encapsulated into lipid–protamine–hyaluronic acid (LPH) nanoparticles surface modified with aHSC-targeting AEAA. Nanoparticles loaded with pRLN or miR-30a-5p had hydrodynamic diameters of 130~150 nm and a surface charge of 20~40 mV (Supplementary Fig. 25). Relative to that with PBS, pRLN, miR-30a-5p and pRLN + miR-30a-5p treatments (Fig. 6a) substantially ameliorated CCl_4-induced liver fibrosis, as indicated by a decreased and more homogeneous echogenicity and shrunk ultrasound reflection regions (Fig. 6b,c), as well as lower ECM depositions, expressions of fibrogenesis-associated markers and blood levels of ALT and AST (Fig. 6d–h), with the best efficacy achieved by the combinatorial gene therapy. In particular, pRLN + miR-30a-5p restored both liver enzymes to the normal ranges (AST, 54–298 U l^{-1}; ALT, 17–77 U l^{-1}). Similar to the in vitro outcome, the highest increase of PPAR-γ expression by pRLN + miR-30a-5p treatment (10.8-fold versus PBS) among the different groups (pRLN or miR-30a-5p, 2- or 3.5-fold versus PBS) (Fig. 6f) presumably accounts for the synergistic antifibrosis effect.

Feeding with a choline-deficient, L-amino acid-defined high-fat diet that contains 0.1% methionine (CDAHFD) elicits hepatic steatosis, liver inflammation and fibrosis, which well mimics the pathogenesis of human non-alcoholic steatohepatitis[37,38] and thus was chosen as a clinically relevant model for further in vivo efficacy evaluation (Fig. 7a). In all the treatment groups, a temporary and slight decrease of body weight was observed through the first three weeks after CDAHFD feeding, which then gradually recovered and increased afterwards (Supplementary Fig. 26a). Fat accumulation was confirmed by a dramatic increase of hepatic fat droplets in CDAHFD-fed mice compared with those in healthy controls (Supplementary Fig. 26b). Similar to the CCl_4 model, pRLN + miR-30a-5p most effectively reduced CDAHFD-induced liver fibrosis and injuries among all the treatment groups (Fig. 7b–d,j and Supplementary Fig. 26c,e). Moreover, only the combinatorial treatment alleviated steatosis, as indicated by fewer micro- or macrovesicular lipid droplets in the liver compared with those in the PBS treatment (Supplementary Fig. 26b,d). Flow cytometric analyses of viable CD45$^+$Ly6G$^-$ cells in the liver demonstrated higher proportions and cell numbers of total macrophages after pRLN or pRLN + miR-30a-5p treatment relative to those after PBS treatment (Fig. 7e,f and Supplementary Figs. 15b and 27). In particular, only treatments that involved pRLN replenished Kupffer cells, decreased Ly6c^{hi} and increased Ly6c^{lo} fractions in monocyte-derived macrophages (CD11b high and F4/80 intermediate expression (CD11b^{hi}F4/80^{mid}) subset) (Fig. 7e,g,h). FACS CD45$^+$Ly6G$^-$CD11b^{hi}F4/80^{mid} cells further downregulated Ly6C, CD86 and TIMPs, but upregulated MMP9, Nur77 and miR-30a-5p expressions after pRLN or pRLN + miR-30a-5p treatment (Fig. 7i), which supports that pRLN, but not miR-30a-5p, drives the

Fig. 5 | MiR-30a-5p in exosomes derived from RLN-educated macrophages deactivates aHSCs by targeting ASK1. a, Heatmap output for miRNA arrays of exosomes derived from the CM of IFN-γ + LPS-stimulated Raw264.7 cells after PBS or RLN treatment. Values represent $\log_{10}2^{-\Delta Ct}$, where the change in threshold cycle $\Delta Ct = Ct_{miRNA} - Ct_{control_miRNA}$. Ct, threshold cycle. **b**, Scatter plot with cutoff at threefold within exosomes derived from the CM of PBS- or RLN-treated Raw264.7 cells. The red arrow indicates the most highly enriched exosomal miR-30a-5p from RLN-treated Raw264.7 cells. The other five upregulated and enriched miRNAs after RLN treatment (miR-27b-3p, miR-150-5p, miR-132-3p, miR-378-3p and miR-744-5p) are highlighted in **a** by black arrows. **c**, Heatmap of integrated scores that predict the association between miRNAs with fibrosis-associated genes. Higher scores indicate a better association. **d**, Relative expression of miR-30a-5p in CCl_4-induced fibrotic livers from mice treated with PBS, pRLN LPD, CloLipo or pRLN LPD + CloLipo following the schedule in Fig. 3a. **e**, Relative mRNA expression of ASK1, PDGF-a, MMP1, MMP13 and TIMP1 in TGF-β activated LX-2 cells at 24 h after various combination treatments of RLN or PBS (indicated by '–' for RLN) with the miR-30a-5p mimic or scrambled-miR mimic (indicated by '–' for miR-30a-5p) ($n = 4$ biologically independent samples per group). **f**, Western blot analysis of ASK1, pASK1, collagen I and α-SMA expression in untreated LX-2 cells or TGF-β-activated LX-2 cells at 48 h after various combination treatments of RLN or PBS with the miR-30a-5p mimic or scrambled-miR mimic. Data shown represent one of three experiments with similar results. Cumulative densitometric analyses of the western blotting images were performed by ImageJ ($n = 4$ biologically independent samples per group). **g**, Relative mRNA expression of PPAR-γ in TGF-β-activated LX-2 cells at 24 h after various combination treatments of RLN or PBS with the miR-30a-5p mimic or scrambled-miR mimic ($n = 4$ biologically independent samples per group). **h**, Relative miR-30a-5p expression in Raw264.7 cells without treatment (PBS), transfected with the miRiCtr or miR30i, or with the combination treatment of miR30i and RLN (miR30i + RLN) ($n = 5$ biologically independent samples per group). **i**, Western blot analysis of collagen I and α-SMA expression in activated HSC-T6 cells after treatment with exosomes collected via ultracentrifugation of the CM from Raw264.7 cells treated with miRiCtr, miRiCtr + RLN, miR30i and miR30i + RLN. Cumulative densitometric analyses of the western blotting images were performed by ImageJ ($n = 5$ biologically independent samples per group). **j**, Relative mRNA expression of TGF-β, PDGF-a, MMP13 and TIMP1 in activated HSC-T6 cells after treatment with exosomes collected via ultracentrifugation of the CM from Raw264.7 cells treated with miRiCtr, miRiCtr + RLN, miR30i and miR30i + RLN ($n = 5$ biologically independent samples per group). Experiments were repeated twice independently with similar results. Significant differences were assessed using a one-way ANOVA with Turkey test. Results are presented as mean ± s.d. from the second repeat. GADPH, glyceraldehyde 3-phosphate dehydrogenase.

phenotype switch of recruited macrophages. Finally, a significant regulation of fibrogenesis-associated genes in the whole liver was observed after either pRLN or miR-30a-5p monotherapy (Fig. 7j). As miR-30a-5p was specifically delivered into aHSCs, this result proved that miR-30a-5p promotes resolution of liver fibrosis by directly targeting aHSCs, not via macrophages.

Neither proposed gene therapies induced a histological abnormity in the major organs, nor caused any significant changes in body weight, creatinine, blood urea nitrogen or blood cell counts compared with those in the PBS treatment (Supplementary Figs. 26a and 28a,b), which suggests negligible systemic toxicity and low immunogenicity. The systemic application of recombinant RLN

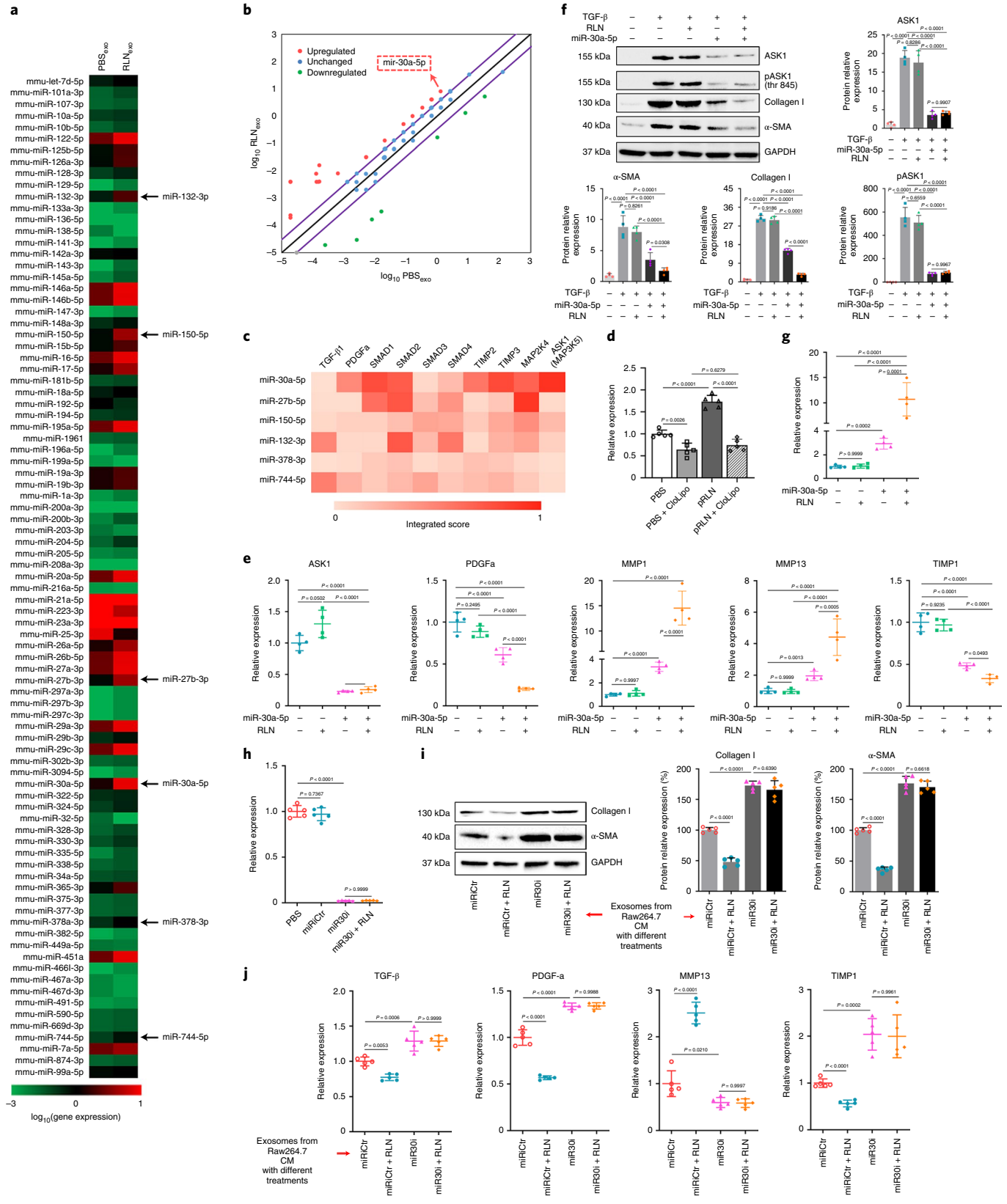

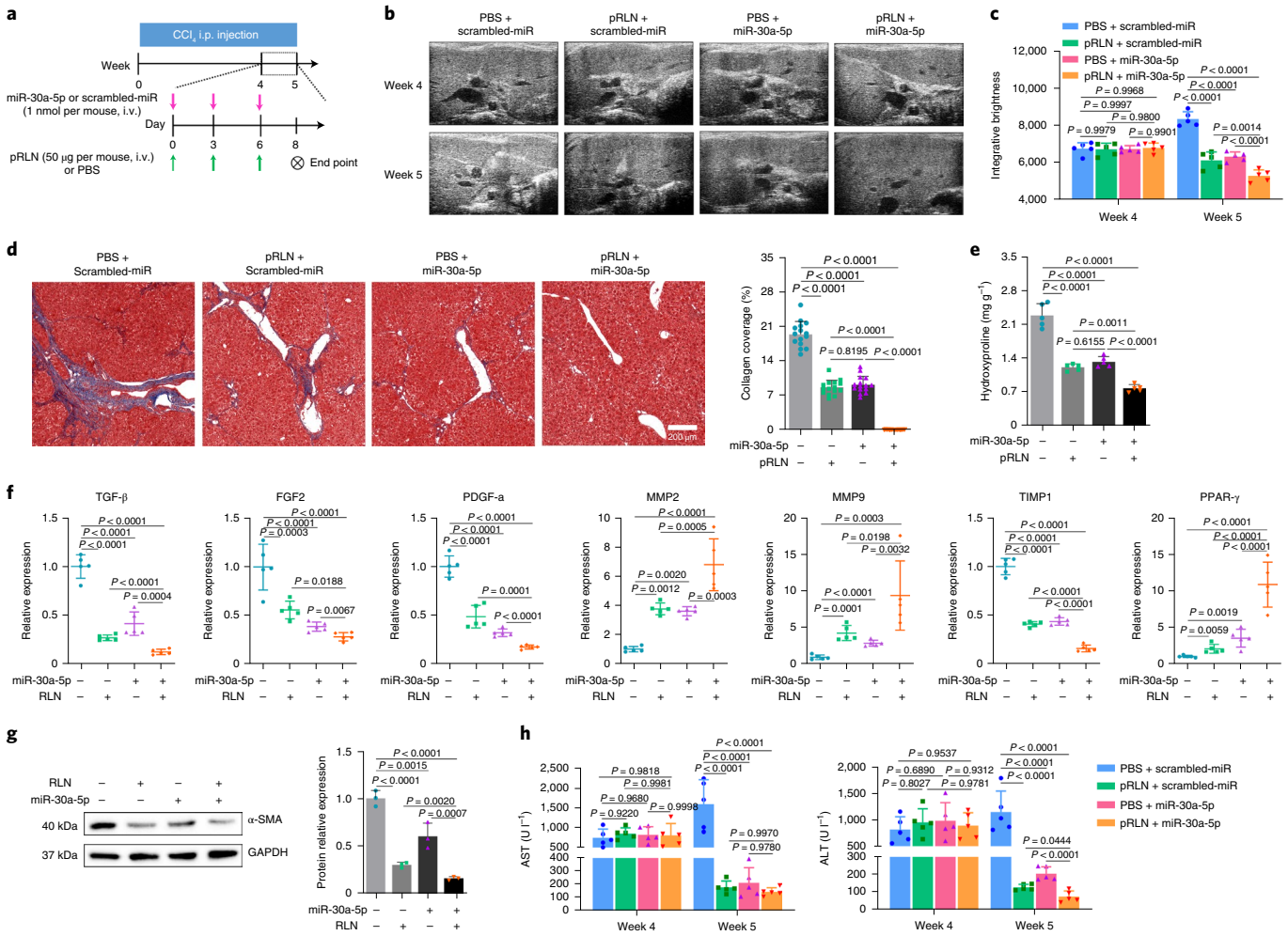

Fig. 6 | Combination of pRLN LPD with miR-30a-5p LPH achieves a synergistic antifibrosis effect in the CCl_4-induced liver fibrosis model. a, Schematic representation of the CCl_4-induced liver fibrosis model and treatment timeline for PBS, pRLN LPD and miR-30a-5p or scrambled-miR LPH. **b**, Representative in vivo ultrasound imaging of mice livers from different treatment groups at weeks 4 and 5 after the initiation of CCl_4 injections. **c**, Quantification analysis of liver fibrosis severity by the integrated intensity of echogenicity (image brightness) ($n = 5$ biologically independent mice per group). **d**, Representative Masson's trichrome staining in CCl_4-induced fibrotic livers from different groups at the end point. Quantification of the average percentage collagen coverage was performed in three randomly selected fields per sample by ImageJ ($n = 5$ biologically independent mice per group). **e**, Quantification of hepatic hydroxyproline content. The data are expressed as hydroxyproline (mg) per liver wet weight (g) ($n = 5$ biologically independent mice per group). **f**, Relative mRNA expression of TGF-β, FGF2, PDGF-a, MMP2, MMP9, TIMP1 and TIMP2 in CCl_4-induced fibrotic livers from mice that received combinational treatments of RLN or PBS (indicated by '−' for RLN) with the miR-30a-5p mimic or scrambled-miR mimic (indicated by '−' for miR-30a-5p) ($n = 5$ biologically independent mice per group). **g**, Western blot analysis of α-SMA expression in CCl_4-induced fibrotic livers from different treatment groups. Cumulative densitometric analyses of the western blotting images were performed by ImageJ ($n = 3$ biologically independent mice per group). **h**, Liver injury characterization by serum AST (left) and ALT (right) in mice from various treatment groups at weeks 4 and 5 after the initiation of CCl_4 injections ($n = 5$ biologically independent mice per group). Experiments were repeated twice independently with similar results. Significant differences were assessed using a two-way ANOVA with Turkey test (**c**,**h**) and a one-way ANOVA with Turkey test (**d**–**g**). Results are presented as mean ± s.d. from the second repeat.

commonly causes bleeding tendency due to suppression of the platelet release and impaired platelet aggregation[39,40], which increases the risk of mortality during diagnostic or therapeutic invasive procedures and causes a notable safety issue for cirrhosis patients as they are commonly diagnosed with impaired blood coagulation capacity[41,42]. We proved that, unlike recombinant RLN, RLN gene therapy did not prolong tail bleeding time (Supplementary Fig. 28c and Supplementary Videos 1–3). Overall, RLN gene therapy is safe and its antifibrosis effect can be further potentiated by the enforced upregulation of miR-30a-5p in aHSCs.

Conclusions

Through cooperating nanotechnology and basic science, we identified macrophages as a central hub to fulfil aHSC deactivation for the treatment of liver fibrosis with RLN (Supplementary Fig. 29). Previous antifibrotic strategies mainly focused on blocking monocyte recruitment via the antagonism of CCL2 or CCL5[43–45] to limit the generation of pro-inflammatory and fibrogenic macrophages. Unfortunately, these therapies also ended up with the retardation of fibrosis resolution due to an adverse impact on the development of pro-resolution macrophages[5]. Intrahepatically enforced expression of RLN provides a new direction by promoting macrophage infiltration and meanwhile 'push' the pro-inflammatory macrophages to turn into the pro-resolution phenotype through Nur77 activation. More importantly, we found that, despite the enhanced RXFP1 expression on aHSCs, they are inert to RLN treatment, presumably due to the highly upregulated stress-activated protein kinase (ASK1)[35] in response to profibrogenic activation, which suppresses

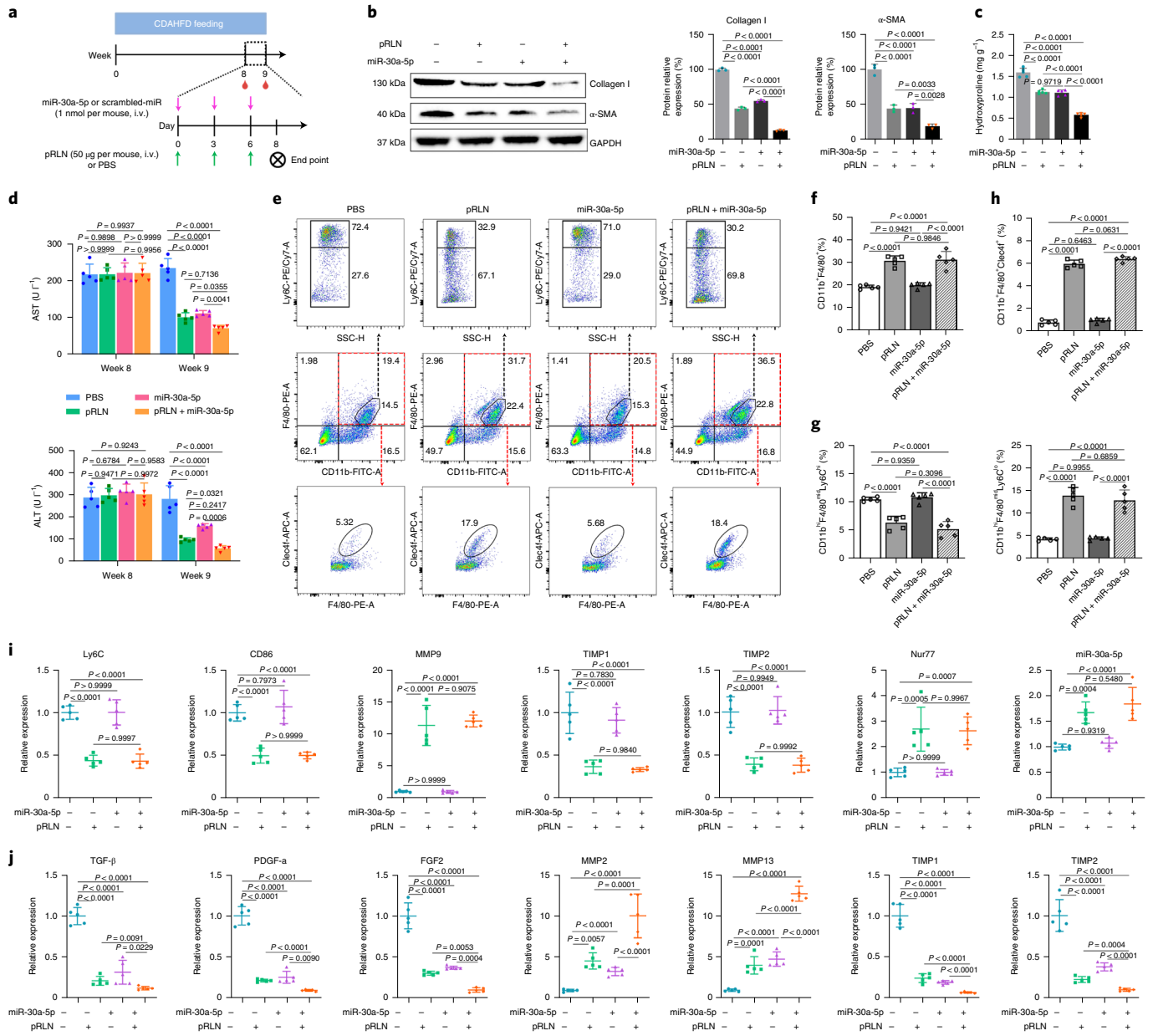

Fig. 7 | The combination of pRLN LPD with miR-30a-5p LPH achieves a synergistic antifibrosis effect in a CDAHFD-induced steatohepatitis model. a, Schematic representation of CDAHFD diet-induced steatohepatitis model and treatment timeline for PBS or pRLN LPD, and miR-30a-5p or scrambled-miR LPH. Blood sampling was performed before the beginning of week 8 and after the beginning of week 9 for various treatments. **b**, Western blot analysis of collagen I and α-SMA expression in fibrotic livers from different treatment groups. Cumulative densitometric analyses of the western blotting images were performed by ImageJ ($n = 3$ biologically independent mice per group). **c**, Quantification of hepatic hydroxyproline content. The data are expressed as hydroxyproline (mg) per liver wet weight (g) ($n = 5$ biologically independent mice per group). **d**, Liver injury characterization by serum AST (top) and ALT (bottom) in mice from various treatment groups at weeks 8 and 9 after CDAHFD feeding ($n = 5$ biologically independent mice per group). **e**–**h** Representative flow cytometry results (**e**) and percentages of $CD11b^+F4/80^+$ total macrophages (**f**) and the $Ly6C^{hi}$ (left), $Ly6C^{lo}$ (right) (**g**) and the resident macrophage (**h**) subsets in fibrotic livers after various treatments ($n = 5$ biologically independent mice per group). **i**, Relative miR-30a-5p and mRNA expression of Ly6C, CD86, MMP9, TIMP1, TIMP2 and Nur77 in FACS bone-marrow-derived macrophages ($CD45^+Ly6G^-CD11b^{hi}F4/80^{mid}$ cells) from mice livers that received combinational treatments of pRLN or PBS (indicated by '–' for RLN) with the miR-30a-5p mimic or scrambled-miR mimic (indicated by '–' for miR-30a-5p) ($n = 5$ biologically independent mice per group). **j**, Relative mRNA expression of TGF-β, PDGF-a, FGF2, MMP2, MMP13, TIMP1 and TIMP2 in fibrotic livers from mice that received combinational treatments of pRLN or PBS (indicated by '–' for RLN) with the miR-30a-5p mimic or scrambled-miR mimic (indicated by '–' for miR-30a-5p) ($n = 5$ biologically independent mice per group). Experiments were repeated twice independently with similar results. Significant differences were assessed using a two-way ANOVA with Turkey test (**d**) and a one-way ANOVA with Turkey test (**b**,**c**,**f**–**j**). Results are presented as mean ± s.d. from the second repeat.

the RLN-RXFP1 downstream effector (PPAR-γ). Nevertheless, exosomal miR-30a-5p released from the RLN-educated pro-resolution macrophages allows us to suppress ASK1 expression and hence revive the RLN-mediated PPAR-γ activation and antifibrosis effect in aHSCs. We delineated the sequential steps of the RLN-induced macrophage phenotype switch and followed the crosstalk between

pro-resolution macrophages and aHSCs to provide a combinatory gene therapy (pRLN + miR-30a-5p) that synergistically and safely ameliorates liver fibrosis.

Online content

Any methods, additional references, Nature Research reporting summaries, source data, extended data, supplementary information, acknowledgements, peer review information; details of author contributions and competing interests; and statements of data and code availability are available at https://doi.org/10.1038/s41565-020-00836-6.

Received: 19 February 2020; Accepted: 30 November 2020;
Published online: 25 January 2021

References

1. Troeger, J. S. et al. Deactivation of hepatic stellate cells during liver fibrosis resolution in mice. *Gastroenterology* **143**, 1073–1083. e1022 (2012).
2. Hu, M. et al. Relaxin gene delivery mitigates liver metastasis and synergizes with check point therapy. *Nat. Commun.* **10**, 2993 (2019).
3. Fallowfield, J. A. et al. Relaxin modulates human and rat hepatic myofibroblast function and ameliorates portal hypertension in vivo. *Hepatology* **59**, 1492–1504 (2014).
4. Tacke, F. & Zimmermann, H. W. Macrophage heterogeneity in liver injury and fibrosis. *J. Hepatol.* **60**, 1090–1096 (2014).
5. Ramachandran, P. et al. Differential Ly-6C expression identifies the recruited macrophage phenotype, which orchestrates the regression of murine liver fibrosis. *Proc. Natl Acad. Sci. USA* **109**, E3186–E3195 (2012).
6. Pellicoro, A., Ramachandran, P., Iredale, J. P. & Fallowfield, J. A. Liver fibrosis and repair: immune regulation of wound healing in a solid organ. *Nat. Rev. Immunol.* **14**, 181–194 (2014).
7. Francis, H. et al. Regulation of the extrinsic apoptotic pathway by microRNA-21 in alcoholic liver injury. *J. Biol. Chem.* **289**, 27526–27539 (2014).
8. Chen, S. A. et al. The pharmacokinetics of recombinant human relaxin in nonpregnant women after intravenous, intravaginal, and intracervical administration. *Pharma. Res* **10**, 834–838 (1993).
9. Uhlén, M. et al. Tissue-based map of the human proteome. *Science* **347**, 1260419 (2015).
10. Friedman, S. L. Hepatic stellate cells: protean, multifunctional, and enigmatic cells of the liver. *Physiol. Rev.* **88**, 125–172 (2008).
11. Hu, M. & Huang, L. Nanomaterial manipulation of immune microenvironment in the diseased liver. *Adv. Funct. Mater.* **29**, 1805760 (2019).
12. Kushiyama, T. et al. Alteration in the phenotype of macrophages in the repair of renal interstitial fibrosis in mice. *Nephrology* **16**, 522–535 (2011).
13. Ma, P. F. et al. Cytotherapy with M1-polarized macrophages ameliorates liver fibrosis by modulating immune microenvironment in mice. *J. Hepatol.* **67**, 770–779 (2017).
14. Kern, K. et al. CD200 selectively upregulates prostaglandin E2 and D2 synthesis in LPS-treated bone marrow-derived macrophages. *Prostag. Oth. Lipid Mediat.* **133**, 53–59 (2017).
15. Wang, M. et al. Chronic alcohol ingestion modulates hepatic macrophage populations and functions in mice. *J. Leukoc. Biol.* **96**, 657–665 (2014).
16. Liaskou, E. et al. Monocyte subsets in human liver disease show distinct phenotypic and functional characteristics. *Hepatology* **57**, 385–398 (2013).
17. Zimmermann, H. W. et al. Functional contribution of elevated circulating and hepatic non-classical CD14 + CD16 + monocytes to inflammation and human liver fibrosis. *PloS ONE* **5**, e11049 (2010).
18. Krenkel, O. & Tacke, F. Liver macrophages in tissue homeostasis and disease. *Nat. Rev. Immunol.* **17**, 306–321 (2017).
19. Hanna, R. N. et al. The transcription factor NR4A1 (Nur77) controls bone marrow differentiation and the survival of Ly6C$^-$ monocytes. *Nat. Immunol.* **12**, 778–785 (2011).
20. Mildner, A. et al. Genomic characterization of murine monocytes reveals C/EBPβ transcription factor dependence of Ly6C$^-$ cells. *Immunity* **46**, 849–862. e847 (2017).
21. Palumbo-Zerr, K. et al. Orphan nuclear receptor NR4A1 regulates transforming growth factor-β signaling and fibrosis. *Nat. Med.* **21**, 150–158 (2015).
22. Hsu, S. Y. et al. Activation of orphan receptors by the hormone relaxin. *Science* **295**, 671–674 (2002).
23. Maruoka, H. et al. Dibutyryl-cAMP up-regulates Nur77 expression via histone modification during neurite outgrowth in PC12 cells. *J. Biochem.* **148**, 93–101 (2010).
24. Lough, J., Rosenthall, L., Arzoumanian, A. & Goresky, C. A. Kupffer cell depletion associated with capillarization of liver sinusoids in carbon tetrachloride-induced rat liver cirrhosis. *J. Hepatol.* **5**, 190–198 (1987).
25. Simons, M. & Raposo, G. Exosomes—vesicular carriers for intercellular communication. *Curr. Opin. Cell Biol.* **21**, 575–581 (2009).
26. Valadi, H. et al. Exosome-mediated transfer of mRNAs and microRNAs is a novel mechanism of genetic exchange between cells. *Nat. Cell Biol.* **9**, 654–659 (2007).
27. Kim, K. M., Abdelmohsen, K., Mustapic, M., Kapogiannis, D. & Gorospe, M. RNA in extracellular vesicles. *WIREs RNA* **8**, e1413 (2017).
28. Tokar, T. et al. mirDIP 4.1—integrative database of human microRNA target predictions. *Nucleic Acids Res.* **46**, D360–D370 (2017).
29. Zhang, P. et al. The deubiquitinating enzyme TNFAIP3 mediates inactivation of hepatic ASK1 and ameliorates nonalcoholic steatohepatitis. *Nat. Med.* **24**, 84–94 (2018).
30. Liles, J. T. et al. ASK1 contributes to fibrosis and dysfunction in models of kidney disease. *J. Clin. Investig.* **128**, 4485–4500 (2018).
31. Singh, S., Simpson, R. L. & Bennett, R. G. Relaxin activates peroxisome proliferator-activated receptor γ (PPARγ) through a pathway involving PPARγ coactivator 1α (PGC1α). *J. Biol. Chem.* **290**, 950–959 (2015).
32. Singh, S. & Bennett, R. G. Relaxin signaling activates peroxisome proliferator-activated receptor gamma. *Mol. Cell. Endocrinol.* **315**, 239–245 (2010).
33. Hazra, S., Miyahara, T., Rippe, R. A. & Tsukamoto, H. PPAR gamma and hepatic stellate cells. *Comp. Hepatol.* **3**, S7 (2004).
34. Wei, J. et al. PPARγ downregulation by TGF-β in fibroblast and impaired expression and function in systemic sclerosis: a novel mechanism for progressive fibrogenesis. *PloS ONE* **5**, e13778 (2010).
35. Chibon, F. et al. ASK1 (MAP3K5) as a potential therapeutic target in malignant fibrous histiocytomas with 12q14–q15 and 6q23 amplifications. *Genes Chromosomes Cancer* **40**, 32–37 (2004).
36. Tang, X. et al. An RNA interference-based screen identifies MAP4K4/NIK as a negative regulator of PPARγ, adipogenesis, and insulin-responsive hexose transport. *Proc. Natl Acad. Sci. USA* **103**, 2087–2092 (2006).
37. Xiong, J. et al. hnRNPU/TrkB defines a chromatin accessibility checkpoint for liver injury and nonalcoholic steatohepatitis pathogenesis. *Hepatology* **71**, 1228–1246 (2020).
38. Matsumoto, M. et al. An improved mouse model that rapidly develops fibrosis in non-alcoholic steatohepatitis. *Int. J. Exp. Pathol.* **94**, 93–103 (2013).
39. Bani, D., Bigazzi, M., Masini, E., Bani, G. & Sacchi, T. B. Relaxin depresses platelet aggregation: in vitro studies on isolated human and rabbit platelets. *Lab. Invest.* **73**, 709–716 (1995).
40. Erikson, M. S. & Unemori, E. N. in *Relaxin 2000* (eds Tregear G.W., Ivell R., Bathgate R.A. & Wade J.D.) 373–381 (Springer, 2001).
41. Amitrano, L., Guardascione, M. A., Brancaccio, V. & Balzano, A. Coagulation disorders in liver disease. *Semin. Liver Dis.* **22**, 83–96 (2002).
42. Rios, R., Sangro, B., Herrero, I., Quiroga, J. & Prieto, J. The role of thrombopoietin in the thrombocytopenia of patients with liver cirrhosis. *Am. J. Gastroenterol.* **100**, 1311 (2005).
43. Berres, M. L. et al. Antagonism of the chemokine Ccl5 ameliorates experimental liver fibrosis in mice. *J. Clin. Investig.* **120**, 4129–4140 (2010).
44. Mitchell, C. et al. Dual role of CCR2 in the constitution and the resolution of liver fibrosis in mice. *Am. J. Pathol.* **174**, 1766–1775 (2009).
45. Lefebvre, E. et al. Antifibrotic effects of the dual CCR2/CCR5 antagonist cenicriviroc in animal models of liver and kidney fibrosis. *PloS ONE* **11**, e0158156 (2016).

Publisher's note Springer Nature remains neutral with regard to jurisdictional claims in published maps and institutional affiliations.

© The Author(s), under exclusive licence to Springer Nature Limited 2021

Methods

Materials. *N*-(methoxypolyethylene oxycarbonyl)-1,2-distearoryl-sn-glycero-3-phosphoethanolamine (DSPE-PEG) and 1, 2-distearoyl-sn-glycero-3-phosphoethanolamine-*N*-(amino(polyethylene glycol)-2000) were purchased from the NOF Corporation. *N*-(2-aminoethyl)-4-methoxybenzamide-conjugated DSPE-PEG (DSPE-PEG-AEAA) was synthesized according to a previously established protocol[46] with details provided in Supplementary Methods. 1,2-dioleoyl-3-trimethylammonium-propane chloride salt was purchased from Avanti Polar Lipids, Inc. Clodronate and control liposomes were purchased from Liposoma BV. The MCD diet (A02082002BR) and CDAHFD diet (A06071309, 45 kcal%) was purchased from Research Diets, Inc. Plasmid-encoding mouse relaxin 1 with a Flag tag driven by the cytomegalovirus promoter was prepared by Sino Biological Inc. pGFP driven by the cytomegalovirus promoter was purchased from Bayou Biolabs. Recombinant mouse relaxin 1 peptide (RLN-1) was purchased from LifeSpan BioSciences, Inc. All other chemicals were obtained from Sigma-Aldrich unless otherwise stated.

Human liver samples. Paraffin-embedded liver tissues from male patients with Stage 4 cirrhosis ($n=7$) were provided by the Department of Hepatology at HwaMei Hospital of the University of Chinese Academy of Sciences and approved by the ethics committee. All the patients gave consent for research use of the biospecimens. Liver samples were collected during hepatic resection surgery and the patient identity of the pathological specimens remained anonymous. Among the samples, five were from patients with cirrhosis alone and the other two were from patients with cirrhosis combined with hepatocellular carcinoma.

Experimental mouse model. Eight-week-old male C57BL/6 mice were purchased from the Jackson Laboratory and housed in the specific-pathogen free animal facility with an ambient temperature of 24 ± 2 °C, air humidity of 40–70% and a 12 h dark/12 h light cycle. All the animal testing and research was conducted in compliance with ethical regulations approved by the University of North Carolina (UNC) at Chapel Hill's Institutional Animal Care and Use Committee. For the CCl_4-induced liver fibrosis model, mice received an intraperitoneal injection of a CCl_4/olive oil (7/1, v/v) mixture at a dose of 1 μl g^{-1} twice weekly for 6 weeks[47], during which treatments began after 4 weeks of CCl_4 injections, when an established fibrosis usually develops. Liver injuries were monitored by levels of AST and ALT in the serum 48 h after the injection of CCl_4. In the macrophage depletion study, mice that received 8 injections of CCl_4 were i.v. injected with 10 mg kg^{-1} clodronate or control liposomes every 2 days for a total of 5 injections. For the MCD- or CDAHFD-induced non-alcoholic steatohepatitis model, mice were fed with the MCD or CDAHFD diet for 10 or 9 weeks, during which treatments began from the ninth or eighth week. Liver injuries were monitored by serum AST and ALT levels.

Ultrasound imaging. The development of liver fibrosis was monitored by high-frequency ultrasound imaging using a Visual Sonic Vevo 2100 system. Mice were anaesthetized with 2.5% isoflurane and placed on the heated Vevo mouse-handling table in a supine position. Prewarmed ultrasound transmission gel (Aquasonic 100, Parker Laboratories) was applied to the mouse skin after removing the abdomen fur. Mice were scanned from the ventral body wall using the MS55D real-time MicroScan transducer and the Vevo 2100 imaging system. The livers were imaged in the parasternal long axis view and three measurements of the portal vein area were obtained. The brightness of each echohepatograph was quantified by integrated density using Image J 1.48v.

Preparation and characterization of lipid nanoparticles. pDNA-loaded LPD or miRNA-loaded LPH nanoparticles were prepared through a stepwise self-assembly process based on well-established protocols[48] with details provided in Supplementary Methods. The size and surface charge of the nanoparticles were determined by a Malvern ZetaSizer Nano series.

In vivo gene expression tracking. Five doses of pGFP or pRLN LPDs were i.v. injected every 2 days into mice that bore a CCl_4-induced fibrotic liver. Mice injected with pGFP LPDs were sacrificed 2 days after the final injection and the fibrotic livers were collected and frozen sections made, which were stained with α-SMA fluorescence conjugated antibody and DAPI. Stained frozen sections were analysed for cellular GFP expression using a confocal microscope. Quantification of the positive signal was performed using Image J software. Mice injected with pRLN LPDs were killed 2 days after the final injection. Quantifications of the RLN expression in the liver, heart, lung, spleen, kidney and serum was performed using a mouse RLN-1 ELISA kit (BosterBio) according to the manufacturer's protocols after an appropriate titration.

Antifibrosis treatments. Mice that received a CCl_4 injection or were fed with MCD or CDAHFD were randomized blindly into different treatment groups, and the investigator was blinded to the group allocation during the animal experiments. PBS, pGFP LPD (50 μg of pDNA per mouse, i.v.), pRLN LPD (50 μg of pDNA per mouse, i.v.) and recombinant RLN (30 μg kg^{-1} i.v. (ref. [49])), PBS + miRIDIAN miRNA mimic negative control LPH (1 nmol miRNA mimic per mouse, i.v.) (CN-001000-01, Dharmacon), PBS + miRIDIAN mouse miR-30-5p mimic LPH (1 nmol miRNA mimic per mouse, i.v.) (CS-001040-01, Dharmacon), pRLN LPD + miRIDIAN miRNA mimic negative control LPH (50 μg of pDNA + 1 nmol miRNA mimic per mouse, i.v.) and pRLN LPD + miRIDIAN mouse miR-30a-5p mimic LPH (50 μg of pDNA + 1 nmol miRNA mimic per mouse, i.v.) were given at the respective schedules. The in vivo liver fibrosis development for the CCl_4-based model was monitored using the Vevo 2100 system once per week. Mice in each group were killed 2 days after the final treatment to obtain liver samples for immunofluorescence and histological staining, flow cytometry analysis, enzyme-linked immunosorbent assay, western blot and quantitative real-time PCR (qPCR) assays.

Immunofluorescence and histological staining. Details on tissue pre-processing for frozen or paraffin-embedded sections and staining procedures are provided in Supplementary Methods. Immunofluorescence staining was performed on frozen sections of the fibrotic livers. The primary, fluorescent primary and secondary antibodies used for staining are listed in Supplementary Table 2. Immunofluorescence images were taken on a laser scanning confocal microscope (Zeiss LSM 700) with Zeiss ZEN 2011. Quantification of the positive signals was performed with Image J 1.48v. Histological staining was performed on paraffin-embedded sections from fibrotic livers and other major organs. Masson's trichrome staining was performed following the manufacture's protocols (Abcam). Haematoxylin and eosin staining was conducted at the UNC histology facility. Histological images were taken by using a microscope (Nikon Eclipse Ti-U).

Blood chemistry analysis. Serum was collected by centrifugation of whole blood cell samples at 6,000 r.p.m. at 4 °C for 15 min. Whole blood cellular components and creatinine, blood urea nitrogen, AST and ALT in the serum were counted and assayed at the UNC histology facility.

Bleeding tendency measurement. The bleeding time was measured with the transection of the tail in mice treated with different therapies. A sharp cut of 2 mm from the tail tips of the mice was made 24 h after the final treatment of PBS, recombinant RLN or pRLN LPD i.v. The tails were immediately placed into a tube filled with saline and kept at 37 °C to measure the bleeding times. The bleeding time was recorded as the complete halt of bleeding for at least 10 s.

Flow cytometry assay. Fibrotic liver samples were made into single-cell suspensions, and hepatic macrophages and HSCs were quantitatively analysed by flow cytometry after immunofluorescence staining—the details are provided in Supplementary Methods. After staining, cells were either sorted via FACSArio II or fixed with 4% paraformaldehyde and analysed via BD LSR II or LSRFortessa. The fluorescence conjugated antibodies used for the analysis are listed in Supplementary Table 2. All the data were acquired with a BD FACSDIVA v8.0.1 and analysed via FlowJo V10 (TreeStar).

Cell culture. Human HSC line LX-2 and rat HSC-T6 cell line were purchased from Sigma-Aldrich. Human primary HSCs were purchased from iXCells Biotechnologies. Fresh human peripheral blood mononuclear cells were purchased from STEMCELL Technologies Inc. The murine skin fibroblast cell line (L929), murine macrophage cell line (Raw264.7) and human monocytic cell line (THP-1) were obtained from the Tissue Culture Facility at the UNC Lineberger Comprehensive Cancer Center. All the cell lines tested negative for mycoplasma contamination. LX-2, HSC-T6, Raw264.7 and L929 cells were cultured in high glucose DMEM (Gibco) supplemented with 10% fetal bovine serum (FBS) (Gibco) and 1% antibiotic–antimycotic (Gibco) at 37 °C and 5% CO_2 in a humidified atmosphere. Human primary HSCs were cultured in stellate cell growth medium (iXCells Biotechnologies) supplemented with 10% FBS and 1% antibiotic–antimycotic at 37 °C and 5% CO_2 in a humidified atmosphere. Human primary bone marrow-derived mononuclear cells (hBMMCs) (ATCC PCS-800-013) and THP-1 cells were cultured in a fully supplemented RPMI1640 cell culture medium that contained 10% heat-inactivated FBS, 1% antibiotic–antimycotic and 0.05 nM 2-mercaptoethanol at 37 °C and 5% CO_2 in a humidified atmosphere. BMDMs were collected from adult C57BL/6 male mice and prepared following an established protocol[50], with details provided in Supplementary Methods. The bone marrow derived cells were cultured at 37 °C and 5% CO_2 in a humidified atmosphere for 7 days to differentiate into BMDMs. BMDMs were further polarized with 100 ng ml^{-1} LPS (InvivoGen) and 50 ng ml^{-1} IFN-γ (BioLegend) for 24 h in a fresh DMEM culture medium. Likewise, pro-inflammatory Raw264.7 cells were obtained after 24 h of differentiation in a DMEM culture medium that contained 400 ng ml^{-1} LPS and 2.5 ng ml^{-1} IFN-γ. THP-1 monocytes were differentiated into macrophages by a 24 h incubation with 100 ng ml^{-1} phorbol 12-myristate 13-acetate in the RPMI1640 culture medium followed by a resting period of 24 h in fresh RPMI1640 medium. The macrophages were further polarized into pro-inflammatory phenotype by stimulation with 50 ng ml^{-1} IFN-γ. Human primary bone marrow-derived macrophages were generated by culturing hBMMC in complete RPMI 1640 medium that contained 20 ng ml^{-1} granulocyte macrophage colony-stimulating factor for 6 days. After discarding floating cells,

adherent bone marrow derived macrophages (hBMDMs) were further polarized into the pro-inflammatory phenotype by stimulation with 100 ng ml^{-1} LPS and 50 ng ml^{-1} IFN-γ for 24 h in the fresh RPMI 1640 medium. Activated LX-2 or HSC-T6 cells were obtained by 24 h of stimulation with 10 ng ml^{-1} TGF-β (Cell Signaling Technology).

In vitro transfection studies. For the siRNA transfection, overnight cultured Raw264.7 cells (2.0×10^5 per well) were transfected with 2.3 nM of MISSION mouse Nur77 siRNA (SASI_Mm01_00077215, Sigma-Aldrich), MISSION mouse RXFP1 siRNA (SASI_Mm01_00044309) or MISSION siRNA Universal Negative Control (SIC001, Sigma-Aldrich) using the INTERFERin transfection reagent (Polyplus-transfection) in a DMEM culture medium supplemented with 10% FBS, according to the manufacturer's instructions. After 4 h, 100 ng ml^{-1} of recombinant mouse RLN-1 was added into the culture medium, and the cells were incubated at 37 °C and 5% CO_2 in a humidified atmosphere for 24 h followed by qPCR analysis.

For the miRNA transfection, TGF-β-activated LX-2 (or HSC-T6) cells (1.5×10^5 per well) were transfected with 25 nM miRIDIAN human miR-30a-5p mimic (or miRIDIAN rat miR-30a-5p mimic for HSC-T6 cells) (CS-001040-01, Dharmacon) or 25 nM miRIDIAN miRNA mimic negative control using the DharmaFECT 1 transfection reagent (Dharmacon) in DMEM culture medium, according to the manufacturer's instructions. After 4 h, 100 ng ml^{-1} of recombinant human RLN-2 (or mouse RLN-1 for the HSC-T6 cells) was added into the culture medium, and the cells were incubated at 37 °C and 5% CO_2 in a humidified atmosphere for 24 h followed by qPCR analysis. For the protein level measurement, the medium was changed with fresh DMEM medium that contained 10% FBS and 1% antibiotic-antimycotic 24 h after the miRNA transfection. Then, the transfected cells were incubated for another 24 h.

For the miRNA hairpin inhibitor transfection, IFN-γ + LPS-stimulated Raw264.7 cells (2.0×10^7 per dish) were transfected with 25 nM miRIDIAN miRNA mmu-miR-30a-5p hairpin inhibitor (IH-310383-07) or 25 nM miRIDIAN miRNA hairpin inhibitor negative Control (IN-001005-01) using the DharmaFECT 3 transfection reagent (Dharmacon) in DMEM culture medium, according to the manufacturer's instructions. Meanwhile, 100 ng ml^{-1} of recombinant mouse RLN-1 was added into the culture medium, and the cells were incubated at 37 °C and 5% CO_2 in a humidified atmosphere for 24 h followed by exosome collection.

Exosome isolation and characterization. CM from Raw264.7 macrophages/differentiated THP-1/hBMDMs grown in 75T flasks (~2×10^7 cells per flask) were collected, and the exosomes were isolated using gradient centrifugation. Briefly, the culture supernatants were sequentially centrifuged at 300*g* for 10 min and 1,000*g* for 20 min, followed by filtration using 0.2 μm syringe filters to remove the cell debris and large vesicles. Then, the cleared sample was spun at 100,000*g* for 1.5 h at 4 °C to pellet the exosomes. The collected exosomes were washed twice with PBS. The total protein level of purified exosomes was measured by the bicinchoninic acid assay (Invitrogen). For the in vivo treatment study, purified exosomes were post-inserted with DSPE-PEG-AEAA (exosomes:DSPE-PEG-AEAA, 1:5 w/w) by incubating at 37 °C for 1 h to promote aHSC-specific distribution. Transmission electron microscopy (JEOL 1230) images of exosomes were acquired after negative staining with 1% uranyl acetate.

miRNA array analysis. Exosomal miRNA was extracted using the miRNeasy Mini Kit (Qiagen) according to the manufacturer's instructions. Isolated total RNA (250 ng) was converted into cDNA with the miScript II reverse transcription reaction using HiSpec Buffer. The cDNA was used as the template in qPCR with the miScript miRNA PCR Array Mouse Fibrosis and miScript SYBR Green PCR Kit (Qiagen). The PCR was run on the 7500 Real-Time PCR System using the following thermocycling parameters: 94 °C for 15 min, 40 cycles at 94 °C for 10 s, 55 °C for 30 s and 70 °C for 30 s, followed by a melting curve analysis.

The data were analysed with the online miScript miRNA PCR array data analysis tool (www.qiagen.com/us/shop/pcr/primer-sets/miscript-mirna-pcr-arrays/#resources). To minimize the potential noise introduced by measurements below the detection threshold, miRNAs with a threshold cycle (Ct) value greater than 35 in all the groups were considered as undetected. Specifically, the expression levels of miRNAs were evaluated by a comparative Ct method after normalization of the global mean of expressed miRNAs to the internal control small RNAs.

qPCR assay. Total RNA was extracted from the fibrotic livers or cells using the RNeasy Mini Kit (Qiagen). cDNA was reverse transcribed using the iScript cDNA Synthesis Kit (BIO-RAD). cDNA (500 ng) was amplified with the TaqMan Gene Expression Master Mix. All the primers for the qPCR reactions are listed in Supplementary Table 3. GAPDH was used as the endogenous control. Reactions were conducted using the 7500 Real-Time PCR System and the data were analysed with the 7500 v2.3.

Western blot. Cell or tissue samples were lysed by a radio-immunoprecipitation assay buffer. The bicinchoninic acid assay (Invitrogen) was used to determine the protein concentration in samples according to the manufacturer's protocols. The protein solution was diluted by sample buffer (4×) that contained the reducing reagent and heated at 95 °C for 5 min. Protein was separated by 4–12% SDS–polyacrylamide gel electrophoresis (Invitrogen), and then transferred to polyvinylidene difluoride membranes (Bio-Rad). The membranes were blocked with 3% bovine serum albumin at room temperature for 1 h and then incubated with primary antibodies overnight at 4 °C. The membranes were washed and further incubated with a secondary antibody (appropriately diluted) at room temperature for 1 h, and then detected using the Pierce ECL Western Blotting Substrate (Thermo Fisher Scientific). GAPDH was used as the control. Image Lab 6.0.1 was used to acquire images. Cumulative densitometric analyses of the western blotting images were performed by ImageJ 1.48v.

Quantification of collagen production. The measurement of collagen content produced by the HSC-T6 cell line was performed using a Sirius Red Collagen Detection Kit (Chondrex) according to the manufacturer's instructions, with details provided in Supplementary Methods.

Hydroxyproline assay. The hepatic hydroxyproline content was measured using a colorimetric hydroxyproline assay kit (Abcam) according to the manufacturer's instructions, with details provided in Supplementary Methods.

cAMP assay. Raw264.7 cells were cultured overnight in 96-well plates at 2×10^4 cells per well, followed by PBS or RLN (100 ng ml^{-1}) stimulation for 12 h at 37 °C in the presence of the phosphodiesterase inhibitors 3-isobutyl-1-methylxanthine (IBMX) (0.5 mM) and rolipram (20 μM). Lysis was then accomplished by incubation with HCl (0.1 M) for 20 min at 4 °C. The samples were diluted twofold with PBS with 0.1% BSA and the intracellular cAMP level was measured by a LANCE cAMP kit (Perkin-Elmer) in a 96-well plate suitable for time-resolved fluorescence measurements, using a SpectraMax M5 plate reader (Molecular Devices). The assay was performed according to the manufacturer's instructions, with the exception of antibody addition to the lysate rather than to the cells.

PKA assay. The Pep Tag non-radioactive cAMP-dependent protein kinase assay kit (Promega) was applied, according to the manufacturer's instructions, to determine the PKA activity in Raw264.7 cells with or without RLN stimulation. Briefly, Raw264.7 cells were cultured overnight in a six-well plate at 1×10^6 cells per well, followed by PBS, H89 (10 μM), RLN (100 ng ml^{-1}) or H89 + RLN treatment for 24 h at 37 °C. Homogenized cells from each group were suspended in extraction buffer and centrifuged at 14,000*g* for 5 min at 4 °C. Supernatant (10 μl) adjusted to a protein concentration of 1.5 mg ml^{-1} was used in an assay for PKA activity.

Statistical analysis. Data are expressed as the mean ± s.d. Statistical significance was determined using a two-tailed unpaired Student's *t*-test when only two value sets were compared or by ANOVA for comparison between multiple groups via GraphPad Prism 7.04v. Exact *P* values are documented in the figures or figure legends. No exclusion criteria were incorporated in the design of the experiments for this study.

Reporting summary. Further information on research design is available in the Nature Research Reporting Summary linked to this article.

Data availability

The MicroRNA Data Integration Portal was used to identify gene targets for exosomal miRNAs and can be accessed with http://ophid.utoronto.ca/mirDIP[28]. All data supporting the findings of this study are available within the article and its Supplementary Information. Source data are provided with this paper.

References

46. Banerjee, R., Tyagi, P., Li, S. & Huang, L. Anisamide-targeted stealth liposomes: a potent carrier for targeting doxorubicin to human prostate cancer cells. *Int. J. Cancer* **112**, 693–700 (2004).
47. Constandinou, C., Henderson, N. & Iredale, J. P. in *Fibrosis Research: Methods and Protocols* (eds Varga, J., David A. Brenner, D. A. & Phan, S. H.) 237–250 (Springer, 2005).
48. Wang, Y. et al. Nanoparticle-mediated HMGA1 silencing promotes lymphocyte infiltration and boosts checkpoint blockade immunotherapy for cancer. *Adv. Funct. Mater.* **28**, 1802847 (2018).
49. Teerlink, J. R. et al. Serelaxin, recombinant human relaxin-2, for treatment of acute heart failure (RELAX-AHF): a randomised, placebo-controlled trial. *Lancet* **381**, 29–39 (2013).
50. Ying, W., Cheruku, P. S., Bazer, F. W., Safe, S. H. & Zhou, B. Investigation of macrophage polarization using bone marrow derived macrophages. *J. Vis. Exp.* **76**, e50323 (2013).

Acknowledgements

We thank S. Li for helpful discussions regarding the flow cytometry analysis on hepatic macrophages. The work in LH.'s lab was supported by NIH grants DK100664 and CA198999, and by a grant from Eshelman Institute for Innovation. Human sample collection and procession was done by J.T.'s lab and supported by Huamei Research

Foundation (Grant 2017HMKY07), the Medicine and Health Sciences Research Foundation of Zhejiang Province (Grant 2019KY177).

Author contributions

M.H. and L.H. conceived and designed the research. M.H., Y.W., Z.L., Z.Y., K.G., M.L. and M.W. performed the in vivo mouse experiments. J.T. provided paraffin-embedded liver tissues from patients. M.H. and Y.W. prepared the frozen sections, immunofluorescence and histological staining. M.H. and Y.W. analysed and quantified the microscopic images. M.H. and Y.W. purified the liver macrophage and mononuclear cells, did the flow cytometry assay and analysed the results. M.H. and Y.W. performed the western blot and qPCR assays on the cell and tissue samples. M.H. and Y.W. did the hydroxyproline assay on liver tissues. M.H. isolated and cultured the primary bone marrow-derived macrophages. M.H. designed the in vitro experiments to analyse the interaction between the macrophages and aHSCs. M.H., Y.W. and Z.L. isolated exosomes from Raw264.7 cells, hBMDMs, and differentiated THP-1 cells. M.H. performed miRNA array analyses. M.H. and Y.W. prepared lipid nanoparticles and characterized the exosomes and lipid nanoparticles. M.H., Y.W., K.G. and M.W. analysed the data. M.H. and L.H. wrote the manuscript.

Competing interests

The authors declare no competing interests.

Additional information

Supplementary information is available for this paper at https://doi.org/10.1038/s41565-020-00836-6.

Correspondence and requests for materials should be addressed to L.H.

Peer review information *Nature Nanotechnology* thanks Frank Tacke and the other, anonymous, reviewer(s) for their contribution to the peer review of this work.

Reprints and permissions information is available at www.nature.com/reprints.

nature research

Corresponding author(s): Leaf Huang

Last updated by author(s): Nov 1, 2020

Reporting Summary

Nature Research wishes to improve the reproducibility of the work that we publish. This form provides structure for consistency and transparency in reporting. For further information on Nature Research policies, see our Editorial Policies and the Editorial Policy Checklist.

Statistics

For all statistical analyses, confirm that the following items are present in the figure legend, table legend, main text, or Methods section.

n/a	Confirmed	
☐	☒	The exact sample size (*n*) for each experimental group/condition, given as a discrete number and unit of measurement
☐	☒	A statement on whether measurements were taken from distinct samples or whether the same sample was measured repeatedly
☐	☒	The statistical test(s) used AND whether they are one- or two-sided *Only common tests should be described solely by name; describe more complex techniques in the Methods section.*
☐	☒	A description of all covariates tested
☐	☒	A description of any assumptions or corrections, such as tests of normality and adjustment for multiple comparisons
☐	☒	A full description of the statistical parameters including central tendency (e.g. means) or other basic estimates (e.g. regression coefficient) AND variation (e.g. standard deviation) or associated estimates of uncertainty (e.g. confidence intervals)
☐	☒	For null hypothesis testing, the test statistic (e.g. *F*, *t*, *r*) with confidence intervals, effect sizes, degrees of freedom and *P* value noted *Give P values as exact values whenever suitable.*
☐	☒	For Bayesian analysis, information on the choice of priors and Markov chain Monte Carlo settings
☐	☒	For hierarchical and complex designs, identification of the appropriate level for tests and full reporting of outcomes
☐	☒	Estimates of effect sizes (e.g. Cohen's *d*, Pearson's *r*), indicating how they were calculated

Our web collection on statistics for biologists contains articles on many of the points above.

Software and code

Policy information about availability of computer code

Data collection	Applied Biosystems® 7500 fast and 7500 Real-Time PCR System (7500 v2.3) was used to collect relative gene expression (RQ) values. Visual Sonic Vevo® 2100 system was used for in vivo collection of ultrasound signals of fibrotic livers. Zeiss ZEN 2011 was used to collect confocal images. Image Lab 6.0.1 was used to acquire western blot images. Flow cytometry data were acquired with BD FACSDIVA™ v8.0.1.
Data analysis	Flow cytometry data were analyzed with FlowJo V10. ImageJ 1.48v was used for confocal, western blot, and ultrasound image processing. GraphPad Prism 7.04v was used to analyze the data.

For manuscripts utilizing custom algorithms or software that are central to the research but not yet described in published literature, software must be made available to editors and reviewers. We strongly encourage code deposition in a community repository (e.g. GitHub). See the Nature Research guidelines for submitting code & software for further information.

Data

Policy information about availability of data

All manuscripts must include a data availability statement. This statement should provide the following information, where applicable:

- Accession codes, unique identifiers, or web links for publicly available datasets
- A list of figures that have associated raw data
- A description of any restrictions on data availability

MicroRNA Data Integration Portal (mirDIP) was used to identify gene targets for exosomal miRNAs and can be accessed with http://ophid.utoronto.ca/mirDIP. The authors declare that the data supporting the findings of this study are available within the paper and its supplementary information files.

Field-specific reporting

Please select the one below that is the best fit for your research. If you are not sure, read the appropriate sections before making your selection.

☒ Life sciences ☐ Behavioural & social sciences ☐ Ecological, evolutionary & environmental sciences

For a reference copy of the document with all sections, see nature.com/documents/nr-reporting-summary-flat.pdf

Life sciences study design

All studies must disclose on these points even when the disclosure is negative.

Sample size	Sample size was determined by power analysis (90% power at 5% significance level).
Data exclusions	No exclusion criteria were incorporated in the design of the experiments for this study.
Replication	All experiments were repeated twice or three times as indicated in figure legends with similar results.
Randomization	Groups in all in vitro experiments were selected randomly. Mice receiving 4-week injections of CCl4 or fed with CDAHFD for 8 weeks were randomized blindly into different treatment groups.
Blinding	The investigator was blinded to the group allocation during the animal experiments and in vitro studies. And all analyses were performed by investigators blinded to the experimental conditions.

Reporting for specific materials, systems and methods

We require information from authors about some types of materials, experimental systems and methods used in many studies. Here, indicate whether each material, system or method listed is relevant to your study. If you are not sure if a list item applies to your research, read the appropriate section before selecting a response.

Materials & experimental systems

n/a	Involved in the study
☐	☒ Antibodies
☐	☒ Eukaryotic cell lines
☒	☐ Palaeontology and archaeology
☐	☒ Animals and other organisms
☐	☒ Human research participants
☒	☐ Clinical data
☒	☐ Dual use research of concern

Methods

n/a	Involved in the study
☒	☐ ChIP-seq
☐	☒ Flow cytometry
☒	☐ MRI-based neuroimaging

Antibodies

Antibodies used	The antibodies used in this study were summarized in Supplementary Table 2. The primers for quantitative PCR used in this study were summarized in Supplementary Table 3.
Validation	All antibodies were verified by the supplier and each lot has been quality tested. All the antibodies used are from commercial sources and have been validated by the vendors. Validation data are available on the manufacturer's website. 1. Alexa Fluor® 488 anti-α-SMA has been validated to be used for immunofluorescent staining and flow cytometric analysis and mentioned species reactivity with mouse. (https://www.thermofisher.com/antibody/product/Alpha-Smooth-Muscle-Actin-Antibody-clone-1A4-Monoclonal/53-9760-82) 2. APC anti-F4/80 has been validated to be used for flow cytometric analysis and mentioned species reactivity with mouse. (https://www.biolegend.com/en-us/products/apc-anti-mouse-f4-80-antibody-4071) 3. FITC anti-CD68 has been validated to be used for immunofluorescent staining and mentioned species reactivity with human. (https://www.biolegend.com/en-us/products/fitc-anti-human-cd68-antibody-4844) 4. Anti-RXFP1 has been validated to be used for immunofluorescent staining and Western analysis and mentioned species reactivity with mouse and human. (https://www.rndsystems.com/products/human-mouse-rat-relaxin-r1-antibody-933344_mab8898) 5. Anti-CD63 has been validated to be used for immunofluorescent staining and mentioned species reactivity with mouse. (https://www.biolegend.com/en-us/products/purified-anti-mouse-cd63-antibody-7813) 6. Anti-Nur77 has been validated to be used for immunofluorescent staining and Western analysis and mentioned species reactivity with human. (https://www.cellsignal.com/products/primary-antibodies/nur77-d63c5-xp-rabbit-mab/3960) 7. Anti-α-SMA has been validated to be used for immunofluorescent staining and Western analysis and mentioned species reactivity with mouse and human. (https://www.abcam.com/alpha-smooth-muscle-actin-antibody-1a4-ab7817.html) 8. Anti-Collagen I has been validated to be used for Western analysis and mentioned species reactivity with mouse and human. (https://www.abcam.com/collagen-i-antibody-ab34710.html) 9. Anti-PKA has been validated to be used for Western analysis and mentioned species reactivity with mouse. (https://

www.cellsignal.com/products/primary-antibodies/pka-c-a-antibody/4782)
10. Anti-pCREB (Ser133) has been validated to be used for Western analysis and mentioned species reactivity with mouse. (https://www.cellsignal.com/products/primary-antibodies/phospho-creb-ser133-87g3-rabbit-mab/9198)
11. Anti-ASK1 has been validated to be used for Western analysis and mentioned species reactivity with human. (https://www.cellsignal.com/products/primary-antibodies/ask1-antibody/3762)
12. Anti-ASK1 (Thr845) has been validated to be used for Western analysis and mentioned species reactivity with human. (https://www.cellsignal.com/products/primary-antibodies/phospho-ask1-thr845-antibody/3765)
13. GAPDH antibody has been validated to be used for Western analysis and mentioned species reactivity with mouse and human (https://www.scbt.com/p/gapdh-antibody-fl-335)
14. BV510 anti-CD45 has been validated to be used for flow cytometric analysis and mentioned species reactivity with mouse. (https://www.biolegend.com/en-us/products/brilliant-violet-510-anti-mouse-cd45-antibody-7995)
15. Pacific Blue anti-Ly6G has been validated to be used for flow cytometric analysis and mentioned species reactivity with mouse. (https://www.biolegend.com/en-us/products/pacific-blue-anti-mouse-ly-6g-antibody-6082?GroupID=GROUP20)
16. PE anti-F4/80 has been validated to be used for flow cytometric analysis and mentioned species reactivity with mouse. (https://www.biolegend.com/en-us/products/pe-anti-mouse-f4-80-antibody-4068?GroupID=GROUP20)
17. FITC anti-CD11b has been validated to be used for flow cytometric analysis and mentioned species reactivity with mouse. (https://www.biolegend.com/en-us/products/fitc-anti-mouse-human-cd11b-antibody-347)
18. PE/Cy7 anti-Ly6C has been validated to be used for flow cytometric analysis and mentioned species reactivity with mouse. (https://www.biolegend.com/en-us/products/pe-cyanine7-anti-mouse-ly-6c-antibody-6063)
19. Alexa Fluor® 647 anti-Clec4f has been validated to be used for flow cytometric analysis and mentioned species reactivity with mouse. (https://www.biolegend.com/en-gb/products/alexa-fluor-647-anti-mouse-clec4f-antibody-18329)
20. FITC anti-human CD16 has been validated to be used for flow cytometric analysis and mentioned species reactivity with human. (https://www.biolegend.com/en-us/products/fitc-anti-human-cd16-antibody-567)
21. PE anti-human CD14 has been validated to be used for flow cytometric analysis and mentioned species reactivity with human. (https://www.biolegend.com/en-us/products/pe-anti-human-cd14-antibody-12011)
22. APC anti-human CD56 (NCAM) has been validated to be used for flow cytometric analysis and mentioned species reactivity with human. (https://www.biolegend.com/en-us/products/apc-anti-human-cd56-ncam-antibody-9941)
23. PE/Cy7 anti-human CD66b has been validated to be used for flow cytometric analysis and mentioned species reactivity with human. (https://www.biolegend.com/en-us/products/pe-cyanine7-anti-human-cd66b-antibody-12499)
24. Goat anti-rabbit HRP has been validated to be used as a secondary antibody for rabbit primary antibodies for Western analysis. (https://www.abcam.com/goat-rabbit-igg-hl-hrp-ab205718.html)
25. m-IgGκ BP-HRP has been validated to be used as a secondary antibody for mouse primary antibodies for Western analysis. (https://www.scbt.com/p/m-igg-kappa-bp-hrp)
26. Alexa Fluor® 555 Goat anti-Mouse IgG H&L has been validated to be used as a secondary antibody for mouse primary antibodies for immunofluorescence staining. (https://www.abcam.com/goat-mouse-igg-hl-alexa-fluor-555-ab150114.html)

Eukaryotic cell lines

Policy information about cell lines

Cell line source(s)	LX-2 and HSC-T6 were purchased from Sigma-Aldrich. Human primary hepatic stellate cells were purchased from iXCells Biotechnologies. Fresh human peripheral blood mononuclear cells were purchased from STEMCELL Technologies Inc. L929, Raw264.7, and THP-1 were obtained from Tissue Culture Facility—UNC Lineberger Comprehensive Cancer Center. Human primary bone marrow derived mononuclear cells were purchased from ATCC.
Authentication	None of the cell lines used were authenticated.
Mycoplasma contamination	The cell lines were tested negative for mycoplasma contamination.
Commonly misidentified lines (See ICLAC register)	No cell lines used are listed in the database of commonly misidentified cell lines.

Animals and other organisms

Policy information about studies involving animals; ARRIVE guidelines recommended for reporting animal research

Laboratory animals	Eight-week-old male C57BL/6 mice were purchased from the Jackson Laboratory. Mice were housed in Specific-Pathogen Free animal facility in ambient temperature (24±2 °C), air humidity 40%–70% and 12 h dark/12 h light cycle.
Wild animals	The study did not involve wild animals.
Field-collected samples	The study did not involve samples collected from the filed.
Ethics oversight	All animal handling procedures were approved by the University of North Carolina at Chapel Hill's Institutional Animal Care and Use Committee.

Note that full information on the approval of the study protocol must also be provided in the manuscript.

Human research participants

Policy information about studies involving human research participants

Population characteristics	Liver samples were acquired during hepatic resection surgery. They were from 7 male patients ranging in age from 42 to 65.

Population characteristics	5 samples were from patients with cirrhosis alone and the other 2 were from patients with cirrhosis combined with hepatocellular carcinoma. All subjects give informed consent. All tissue specimens are de-identified.
Recruitment	Eligible patients were invited to participate by one of the investigators or a designee of one of the investigators. If they are willing to participate, the investigator or their designee reviewed the consent form and obtained informed consent. All cirrhosis patients with planned surgery were consented to the liver tissue collection protocol. Patients were approached in clinic by study personnel without relation to age, race, gender, disease stage, or prior therapies. No significant biases appeared to be present.
Ethics oversight	HwaMei Hospital, University of Chinese Academy of Sciences

Note that full information on the approval of the study protocol must also be provided in the manuscript.

Flow Cytometry

Plots

Confirm that:

☒ The axis labels state the marker and fluorochrome used (e.g. CD4-FITC).

☒ The axis scales are clearly visible. Include numbers along axes only for bottom left plot of group (a 'group' is an analysis of identical markers).

☒ All plots are contour plots with outliers or pseudocolor plots.

☒ A numerical value for number of cells or percentage (with statistics) is provided.

Methodology

Sample preparation	Sample preparation listed in Online Methods, 'Flow cytometry assay' section.
Instrument	BD LSR II, LSRFortessa, FACSArio II
Software	BD FACSDIVA™ (Version 8.0.1)
Cell population abundance	Cell count of 20,000 or 8,000,000 events was collected of a relevant cell population after initial gating.
Gating strategy	Initial cell populations were gated for singlet and doublet cells using FSC-A/ FSC-W gating. A near-IR live/dead dye was used to discriminate between viable and dead cells. FMO control stained cells were used to distinguish between background staining and specific antibody staining. Detailed gating strategies were provided within the Supplementary Information.

☒ Tick this box to confirm that a figure exemplifying the gating strategy is provided in the Supplementary Information.